Electronic Supplementary Information (ESI)

Tetracoordinate Co(II) Complexes with Semi-Coordination as Stable Single-Ion Magnets for Deposition on Graphene

Jorge Navarro Giraldo,[a] *Jakub Hrubý,*[a‡] *Šárka Vavrečková,*[ab§] *Ondřej Fellner,*[c] *Lubomír Havlíček,*[ad] *DaVonne Henry,*[e] *Shehan de Silva,*[e] *Radovan Herchel,*[c] *Miroslav Bartoš,*[a] *Ivan Šalitroš,*[a f] *Vinicius T. Santana,*[a] *Paola Barbara,*[e] *Ivan Nemec,**[ac] *and Petr Neugebauer.**[a]

* Corresponding authors

[a] Central European Institute of Technology, CEITEC BUT, Purkyňova 656/123, 61200 Brno, Czech Republic. Email: ivan.nemec@ceitec.vutbr.cz, petr.neugebauer@ceitec.vutbr.cz

[b] Institute of Physical Engineering, Faculty of Mechanical Engineering, Brno University of Technology, Technická 2, 61669 Brno, Czech Republic

[c] Department of Inorganic Chemistry, Faculty of Science, Palacký University, 17. listopadu 12, 77147 Olomouc, Czech Republic

[d] Institute of Physics of Materials, Czech Academy of Sciences, Žižkova 22, 61662 Brno, Czech Republic

[e] Department of Physics, Georgetown University, Washington, DC, United States of America

[f] Department of Inorganic Chemistry, Faculty of Chemical and Food Technology, Slovak University of Technology in Bratislava, Bratislava SK-81237, Slovakia

‡ Present address: National High Magnetic Field Laboratory, Florida State University, 1800 E. Paul Dirac Drive Tallahassee, FL 32310, USA

§ Present address: Institute of Applied Physics, Abbe Center of Photonics, Friedrich Schiller University, Albert-Einstein-Str. 15, 07745 Jena, Germany

Content

Section S1. Experimental Methods

Precursors, Elemental Analysis, Infrared Spectroscopy

$CoCl_2 \cdot 6H_2O$, 2-Amino-6-methylpyridine, Salicylaldehyde, 5-Methylsalicylaldehyde, Triethylamine, solvents (MeOH, diethyl ether (Et_2O) were supplied by VWR International (Stříbrná Skalice, Czech Republic), Sigma-Aldrich (Prague, Czech Republic), Lach-Ner (Neratovice, Czech Republic), Fisher Scientific (Pardubice, Czech Republic), BDL Czech Republic s.r.o. (Turnov, Czech Republic) and Litolab (Chudobín, Czech Republic).

Elemental analysis was performed by Flash 2000 CHNS Elemental Analyzer (Thermo Scientific, Waltham, MA, USA). A Jasco FT/IR-4700 spectrometer (Jasco, Easton, MD, USA) was used for the collection of the infrared (IR) spectra of the studied ligand and complexes in the range of 400-4000 cm^{-1} by using the attenuated total reflection (ATR) technique on a diamond plate.

X-ray Crystallography

Selected single crystals of **1** and **2** were measured using an XtaLAB Synergy-I diffractometer (Rigaku Corporation, Tokyo, Japan) with a HyPix3000 hybrid pixel array detector and a microfocused PhotonJet-I X-ray source (Cu Kα) at 100.0(2) K. The crystal structures were solved using the SHELXT [1] and all non-hydrogen atoms were refined anisotropically on F^2 using and refined by the full matrix least-squares procedure with Olex2.refine [2] in OLEX2 (version 1.5) [3]. All hydrogen atoms were found in differential Fourier maps and their parameters were refined using a riding model with $U_{iso}(H) = 1.2(CH)$ or $1.5(-CH_3)U_{eq}$. To obtain structures suitable for the calculations we finalized their refinement using the non-spherical structure refinement method called Hirshfeld atom refinement [4], [5] incorporated into the module NoSpherA2 (level of theory: B3LYP and def2-TZVPD for **1**, B3LYP and def2-SVP for **2**) [6]. The molecular structures and packing diagram were drawn with MERCURY [7]. In their original report [8], the authors solved the crystal structure of **1** in *Ia* acentric space group. However, our measurements are more consistent with the centrosymmetric space group *I2/a*.

Powder diffraction data were collected using a MiniFlex600 (Rigaku Corporation, Tokyo, Japan) equipped with the Bragg–Brentano geometry, and with iron-filtered Cu $K\alpha_{1,2}$ radiation.

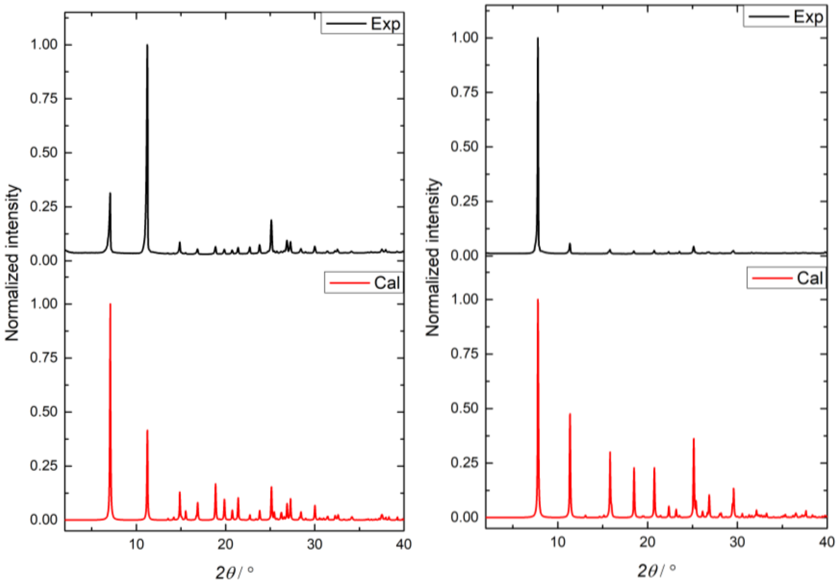

Fig. S1 XRPD data for **1** (left) and **2** (right) obtained using $K\alpha_{1,2}$ Cu irradiation (λ = 1.54056 Å); Black lines: an experimental diffraction pattern, red lines: a pattern calculated from the single-crystal structure.

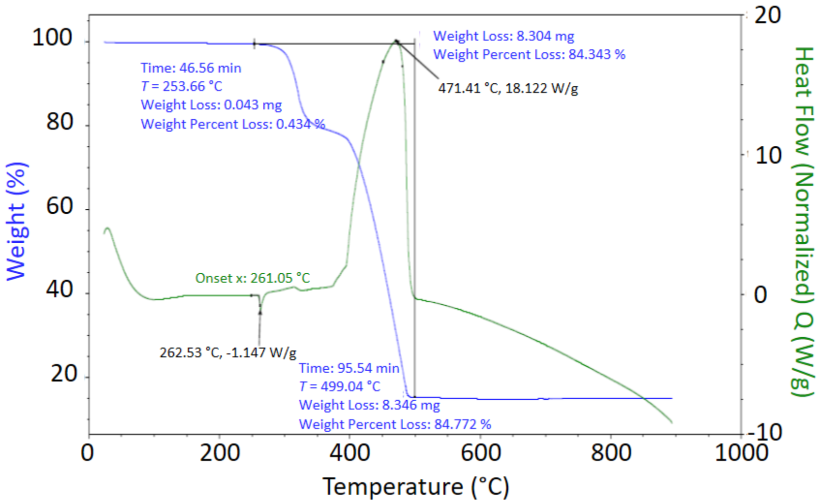

Fig. S2 TG/DSC data measured for **1.**

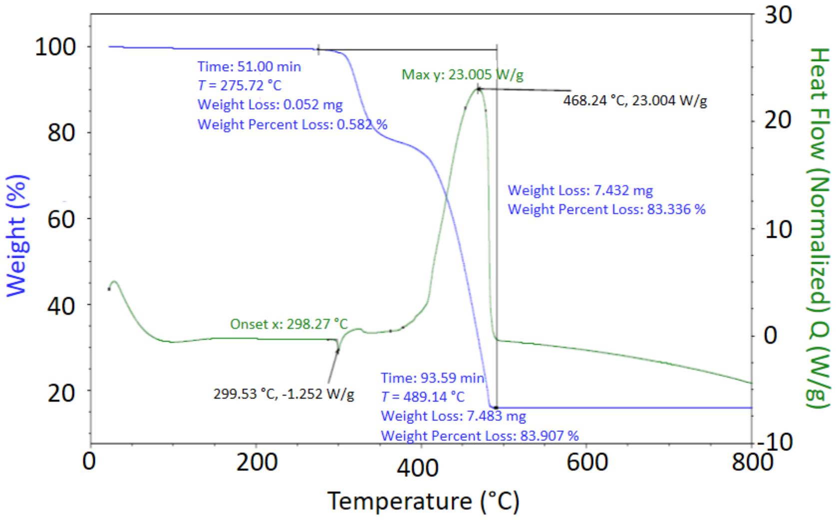

Fig. S3 TG/DSC data measured for **2.**

Table S1 Crystal data and structure refinement for **1** and **2**

	1	**2**
Formula	$C_{26}H_{22}CoN_4O_2$	$C_{28}H_{26}CoN_4O_2$
M_r	481.423	509.477
Crystal system	monoclinic	orthorhombic
Space group	$I2/a$	$Pbcn$
T/K	90.0(2)	90.0(2)
a (Å)	11.7455(1)	25.0976(2)
b (Å)	8.1210(1)	8.0738(1)
c (Å)	22.7458(3)	11.5902(1)
β (°)	98.700(1)	90
V (Å^3)	2144.65(4)	2348.56(4)
Z	4	4
λ (Å), Cu Kα	1.54184	1.54184
D_{calc} (g·cm^{-3})	1.491	1.441

μ (mm^{-1})	6.538	6.002
F (000)	990.326	1054.479
Independent reflections	2095 [R_{int} = 0.0326, R_{sigma} = 0.0162]	2113 [R_{int} = 0.0904, R_{sigma} = 0.0194s]
Data/restraints/parameters	2095/0/249	2113/0/276
Goodness-of-fit on F^2	1.065	1.078
Final R indices [$I > 2\sigma(I)$]	R_1 = 0.0183, wR_2 = 0.0416	R_1 = 0.0222, wR_2 = 0.0580
Final R indices (all data)	R_1 = 0.0190, wR_2 = 0.0419	R_1 = 0.0235, wR_2 = 0.0586
CCDC no.		

Table S2 The results of SHAPE calculation for **1** and **2**

	SP-4	T-4	SS-4	vTBPY-4
1	23.830	2.857	3.800	4.449
2	24.917	2.531	4.723	4.467

SP-4, D_{4h}, Square; T-4, T_d, Tetrahedron; SS-4, C_{2v}, Seesaw; vTBPY-4, C_{3v}, Vacant trigonal bipyramid

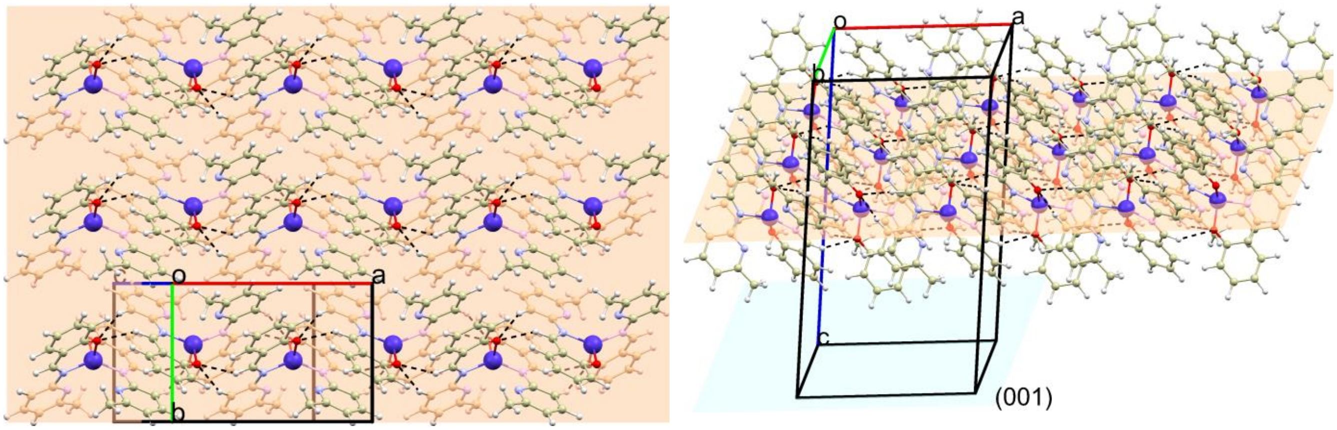

Fig. S4 Perspective views on the supramolecular 2D layers in **1**. The mean plane of the Co atoms is depicted as an apricot-colored plane, while the (001) plane is depicted in blue. Non-covalent interactions are indicated by dashed lines, which are drawn for those interactions where the distance between the donor and acceptor atoms is 0.2 Å shorter than the sum of their van der Waals radii.

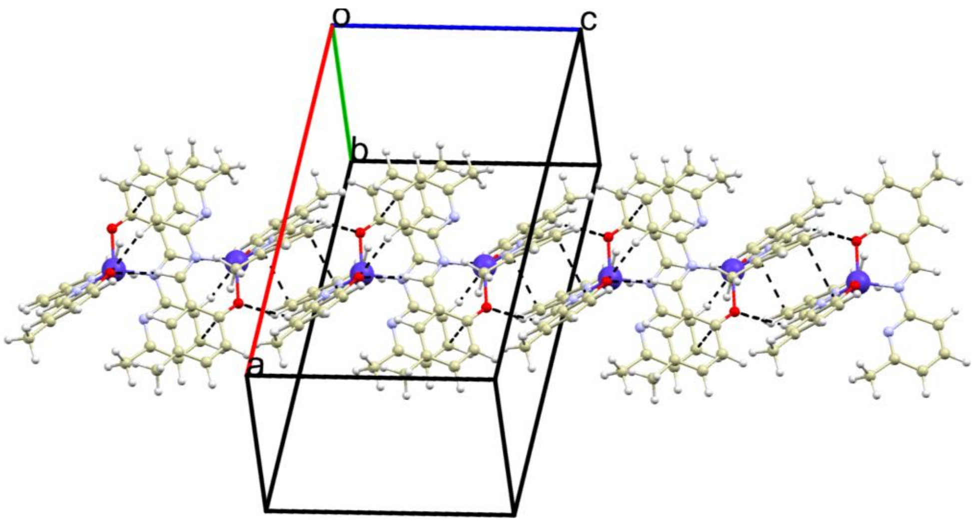

Fig. S5 A perspective view on the supramolecular chain in **2**. Non-covalent interactions are indicated by dashed lines, which are drawn for those interactions where the distance between the donor and acceptor atoms is 0.2 Å shorter than the sum of their van der Waals radii.

Synthesis and Characterization

Complex [Co(salapi)₂] (**1**)

To the solution of 2-amino-6methylpyrdine (4.62 mmol, 500 mg) in 50 mL of methanol 565 mg of salicylaldehyde (4.62 mmol) was added. The solution was heated to 50 ºC, and then, 550 mg of $CoCl_2\cdot 6H_2O$ (2.31 mmol) was added and after five minutes 468 mg of triethylamine (4.62 mmol) was added. The brown-orange solution was refluxed for 30 minutes and 142 mg of red-orange microcrystalline powder were obtained by filtration. Finally, 559 mg of X-ray quality monocrystals were obtained by slow diffusion of Et_2O into filtrate after one day. (Yield = 63%).

Elemental analysis based on $C_{26}H_{22}CoN_4O_2$, M_w = 481.43 g/mol: Anal. Calc. for: C, 64.87; H, 4.61; N, 11.64%; found: C, 64.76; H, 4.59; N, 11.73%.

IR (ATR, v, cm^{-1}): 395w, 460w, 502w, 544w, 605w, 727m, 753m, 786m, 812w, 844w, 911w, 940w, 980w, 1033w, 1096w, 1122w, 1140s, 1182m, 1215w, 1229w, 1285w, 1331m, 1353w, 1385m, 1434s, 1457w, 1522s, 1564m, 1588m, 1603s, 2919w, 3017w, 3050w.

Complex [Co(mesalapi)₂] (**2**)

Compound **2** was prepared using the same procedure as for **1**, but instead of salicylaldehyde the corresponding equivalent of 5-methylsalicylaldehyde was used. The orange X-ray quality crystals of **2** were obtained. (Yield = 58%).

Elemental analysis based on $C_{28}H_{26}CoN_4O_2$; M_w = 509.48 g/mol: Anal. Calc. for: C, 66.01; H, 5.14; N, 11.00%; found: C, 65.75; H, 5.12; N, 10.98%.

IR (ATR, v, cm^{-1}): 390w, 465w, 481w, 514w, 546w, 578w, 729w, 747w, 784m, 824w, 942w, 980w, 1020w, 1135m, 1150m, 1170w, 1202w, 1248w, 1323w, 1381s, 1425s, 1447s, 1520s, 1565m, 1589s, 1602m, 2859w, 2914w, 2995w, 3038w.

Magnetic Measurements

Measurements were collected using a Low-Temperature Vibrating Sample Magnetometer (Cryogenic Limited, London, United Kingdom) with a temperature range 1.6 – 400 K and a magnetic field from 0 to 9 T. The sample was mixed with eicosane and studied in a form of a sphere with a 4 mm diameter. All data were simulated using EasySpin 5.2.33 [9].

Dynamic magnetic investigations have been carried out on MPMS SQUID 3 (Quantum design Inc., San Diego, CA, USA). The exact amount of sample under the study was mixed with melted eicosane and filled into a gelatin capsule, which was used as a sample holder. In the case of magnetic experiments at a static magnetic field, the temperature dependency was recorded in the thermal range 1.9 – 300 K at $B_{\mathrm{DC}} = 0.1$ T using a 1 K/min sweeping rate, and field-dependency was measured at isothermal conditions in the range $B_{\mathrm{DC}} = 0 – 7$ T. Collected data were corrected for the diamagnetism of eicosane and gelatin capsule as well as for the molecular diamagnetic contribution, which was calculated using the Pascal constants [10]. Magnetic functions were transformed into the μ_{eff} vs. T and M_{mol} vs. B dependencies. The experimental details about the ac susceptibility measurements are given in section S7.

High-frequency Electron Spin Resonance (HF-ESR)

HF-ESR spectra were acquired on a home-built spectrometer [11] featuring a signal generator (Virginia Diodes, Charlottesville, USA), an amplifier–multiplier chain (Virginia Diodes, Charlottesville, USA), a quasi-optical bridge (Thomas Keating, Billingshurst, UK), and a 16 T solenoid cryomagnet (Cryogenic, London, UK) with heterodyne signal detection. The reference powder sample of the complex was studied as a pressed powder pellet sample with a diameter of 5 mm. All ESR spectra were simulated using EasySpin 5.2.33 [9].

Section S2. Topological Analysis of the Electron density

Table S3 Topological and energetic properties of $r(\mathbf{r})$ calculated at the selected (3,-1) critical points

	length/Å	$\nabla^2\rho(\mathbf{r})$/a.u.	$h_e(\rho)$/a.u.	$V(\rho)$/a.u.	$G(\rho)$/a.u.	E_{int}/kcal.mol^{-1}	$\lvert V(\rho)\rvert$/G(ρ)
1							
Co1-N1		0.39925	-0.02102	-0.14185	0.12083	44.50	1.17
Co1-O1		0.46142	-0.01698	-0.14932	0.13234	46.85	1.13
2							
Co1-N1		0.40701	-0.02130	-0.14434	0.12305	45.29	1.17
Co1-O1		0.45513	-0.01689	-0.14755	0.13233	46.29	1.12

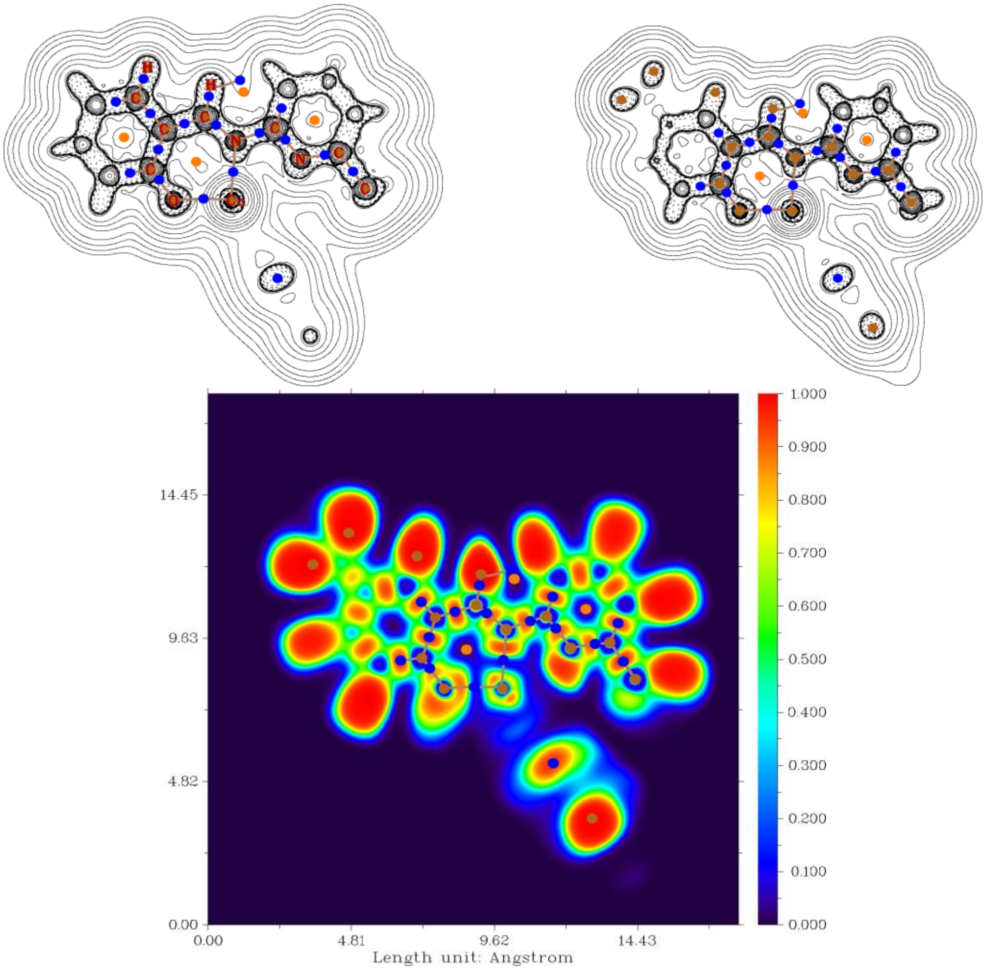

Fig. S6 Laplacian of the electron density $\nabla^2\rho(\mathbf{r})$ calculated for **1** (top left) and **2** (top right). Black lines represent isosurface contour lines, brown lines represent bond pathways, blue circles represent (3,-1) BCPs, dark brown circles represent (3,-3) BCPs, orange circles represent (3,+1) BCPs. (Bottom) Visualization of the electron localization function calculated for **2**.

Section S3. Analysis of Raman Spectroscopy, and XPS of Compound 1 in Bulk and Deposited on Graphene

<u>Deposition of compound **1**</u>

To test the stability of compound **1** during deposition at ambient conditions, it was deposited by drop-casting. The bulk was dissolved in acetone (C_3H_6O, 99%, Penta, Czech Republic) to make a final solution with a 1 mM concentration. The actual drop-casting was conducted in ambient conditions as 40 μL was drop-cast onto a substrate. To test its thermal stability, deposition by thermal sublimation at pressure in the order of 10^{-6} mbar at 270 °C was performed. Thermal sublimation process took 92 hours. Optical and AFM images of the samples deposited by sublimation can be seen in Fig. 5 of the main text, while for drop-cast they are reproduced below.

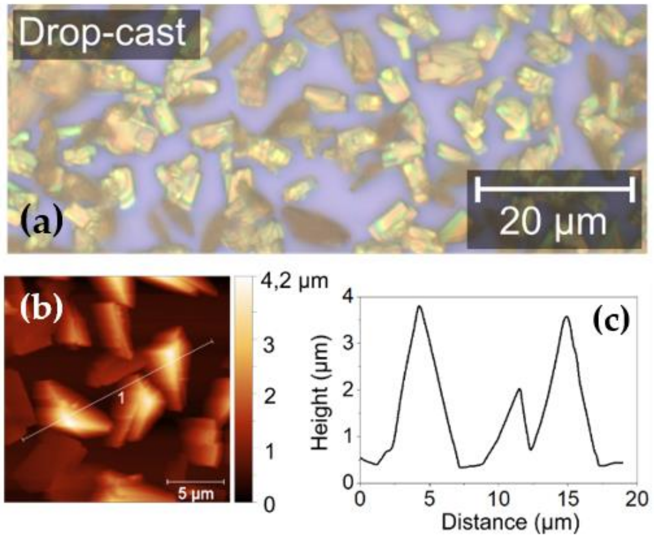

Fig. S7 (a) Optical image of deposited compound 1 (in light green) on CVD graphene (violet background) by drop-cast. (b) AFM image of deposited compound 1 on CVD graphene by drop-cast. (c) The height profile along the white line indicated in the AFM image.

Raman Spectroscopy on Deposited Compound **1**

Raman spectra were acquired on a confocal Raman microscope WITec Alpha300 R+ (WITec, Ulm, Germany). All measurements were carried out with the excitation laser source with a 532 nm wavelength and 1 mW power output.

We performed Raman spectroscopy to investigate the vibrational modes of individual components in the resultant hybrid material and compared to confirm our studied system's intactness. Fig. S8 shows Raman spectra, from top to bottom, of a Si/SiO$_2$ + CVD graphene, bulk compound **1**, and deposited samples by drop-cast and by thermal sublimation. The Si/SiO$_2$ Raman spectrum has a strong phonon band at 519 cm^{-1}, two medium peaks at 301 cm^{-1} and in the region 940–980 cm^{-1}, and a weak peak at 620 cm^{-1} [12], [13]. The spectrum of CVD graphene exhibited strong D peaks at 1346 cm^{-1}, G at 1594 cm^{-1}, and 2D at 2689 cm^{-1}, with the weaker peaks D' at 1622 cm^{-1}, D + D'' at 2464 cm^{-1} and 2D' at 3255 cm^{-1} [14], [15]. The Raman spectrum of the bulk compound contained vibrational bands characteristic of the ligand's functional groups as imino or aromatic C=C/N bonds (ca. 1400–1620 cm^{-1}) or the phenolic group (1200-1300 cm^{-1}) [16]. We chose to use the following most intensive bands for comparison between the bulk and deposited compounds (in cm^{-1}): 1227, 1355, 1385, 1435, 1523, 1563, 1604 and 1612. As seen from Fig. S8, the Raman spectra of hybrid materials prepared either by wet or sublimation techniques confirmed the presence of all of the vibrational peaks observed in the bulk material and all the spectral patterns agree exceptionally well. Therefore, we may conclude that Raman spectroscopy confirmed the stability of compound **1** during the deposition processes. A detailed comparison of peak positions and their intensities is provided in Table S4.

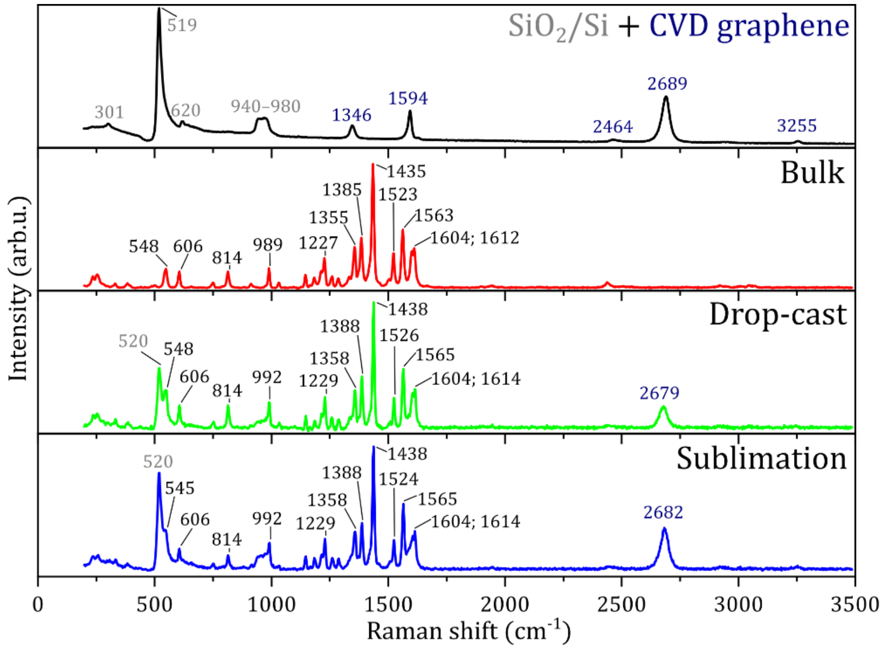

Fig. S8 Comparison of Raman spectra of the compound **1**, from top to bottom, of Si/SiO$_2$ substrate (Raman shift values marked in grey) and CVD graphene (marked in dark blue), bulk, and deposited by drop-cast and by thermal sublimation.

Table S4 Comparison of Raman shift peaks (in cm^{-1}) of Si/SiO$_2$ substrate and CVD graphene, bulk **1**, deposited by drop-cast and by thermal sublimation. Peak intensity is denoted as follows: strong - s, medium - m, weak - w, very weak – vw

SiO$_2$ + CVD graphene	**Bulk 1**	**Drop-cast on CVD graphene**	**Sublimation on CVD graphene**
	238w	240w	238vw
	254w	254w	258vw
301w			307vw
	330vw	332w	332vw
	384vw	386vw	383vw
	445vw	441vw	
	490vw	490vw	
	500vw	500vw	
519s		520s	520s
	548m	548m	545m
	606m	606m	606w
620w			
	660vw	660vw	655vw
	750w	753w	750vw
	814m	814m	814w
	884vw		881vw
	914w		914vw

940-980m		940-980w	945-985w
	989m	992m	992m
	1031w	1034vw	1029vw
	1097vw	1098vw	
	1146w	1147w	1147w
	1168vw	1168vw	1170vw
	1184w	1186w	1183w
	1216w	1214w	1216w
	1227m	1229m	1229m
	1258w	1257w	1260w
	1286w	1287w	1287w
	1334vw	1338w	
1346m	1355m	1358m	1358m
	1385m	1388m	1388m
	1435s	1438s	1438s
	1508vw	1507vw	
	1523m	1526m	1524m
	1563m	1565m	1565s
1594m			
	1604m	1604m	1604m
	1612m	1614m	1614m
1622vw			
	1900vw		
	1943vw	1946vw	1946vw
	2440w	2442vw	2441vw
2464vw			
2689m		2679m	2682m
	2920vw	2914vw	2914vw
2950vw			
	3008vw		
	3046vw	3045vw	3045vw
3255vw		3244vw	3250vw

X-ray Photoelectron Spectroscopy (XPS)

XPS measurements were carried out with a Kratos Axis Supra (Kratos Analytical, Manchester, United Kingdom) spectrometer at room temperature and under ultra-high vacuum (UHV) conditions. The instrument was equipped with a monochromatic Al Kα source of 1486.6 eV (15 mA, 15 kV) and a hemispherical analyzer with a hybrid magnetic and electrostatic lens for enhanced electron collection. Survey and detailed XPS spectra were acquired at normal emission with fixed pass energies of 160 eV and 20 eV, respectively. All spectra were calibrated to the hydrocarbon peak set to 284.8 eV. The Kratos charge neutralizer system was used on all specimens. The inelastic backgrounds in all the spectra were modelled according to the Shirley method [17]. Data analysis was based on a standard deconvolution method using a mixed Gaussian (G) and Lorentzian (L) line shape (G = 70 % and L = 30 %, Gaussian–Lorentzian product) for each component in the spectra. The elemental composition of the samples was evaluated using a semi-empirical approach. The spectra were analyzed using the CasaXPS software (version 2.3.18).

The chemical composition was probed by XPS. Fig. S9 shows the molecular structure of compound **1** with a comparison survey for a bulk powder, bulk powder taken from crucible after sublimation at 270 °C and deposited compound on CVD graphene by thermal sublimation and drop-cast. All spectra exhibited photoelectron peaks Co 2p, N 1s, C 1s, and O 1s and Augers peaks: O$_{KLL}$ and Co$_{LMM}$. In the case of deposited samples also peaks from Si 2p and Si 2s were detected as a Si/SiO$_2$ wafer served as substrate for CVD graphene. All spectra showed compound-specific peaks that corroborate Raman results and imply the preservation of the compound's structure after deposition.

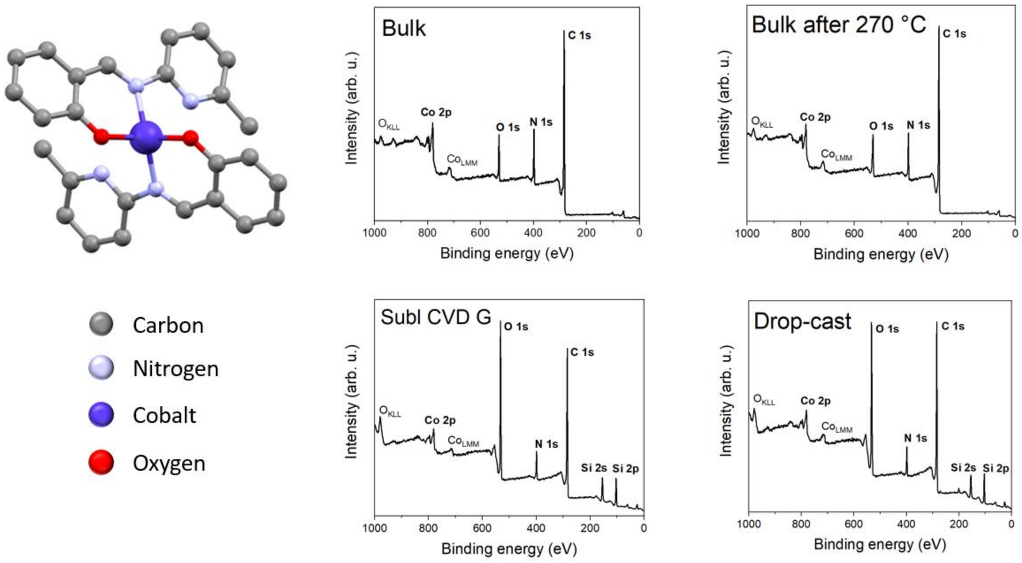

Fig. S9 Compound **1** with XPS survey comparison for bulk, bulk after 270 °C, sublimation on CVD graphene, and drop-cast on CVD graphene.

The detailed spectra (Figs. S10-S13) of the selected peaks revealed specific chemical bonds at their characteristic binding energies. The Co 2p peak exhibited a main component and shake-up satellite, which is a common feature for paramagnetic Co samples [18], [19]. The main components appeared as Co 2p$_{3/2}$ at 796.3 eV and Co 2p$_{1/2}$ at 780.8 eV. The N 1s peak was deconvoluted to three components: pyridinic at 399.1 eV, graphitic at 401.2 eV, and a weak shake-up at 405.7 eV [20]. Detailed spectra of O 1s and C 1s are not shown since samples were exposed to ambient conditions prior to XPS analysis and were affected by adventitious contaminations.

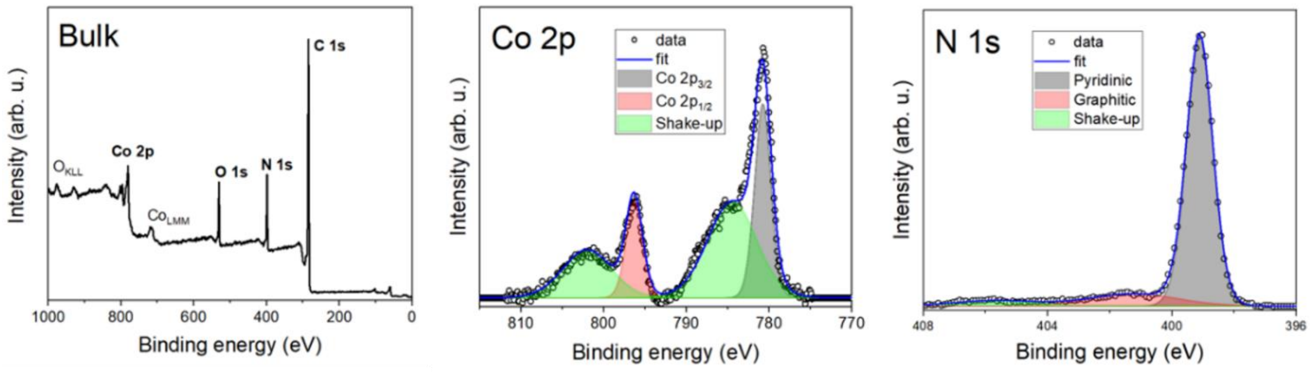

Fig. S10 Survey and detailed XPS spectra of bulk compound **1** for Co 2p and N 1s.

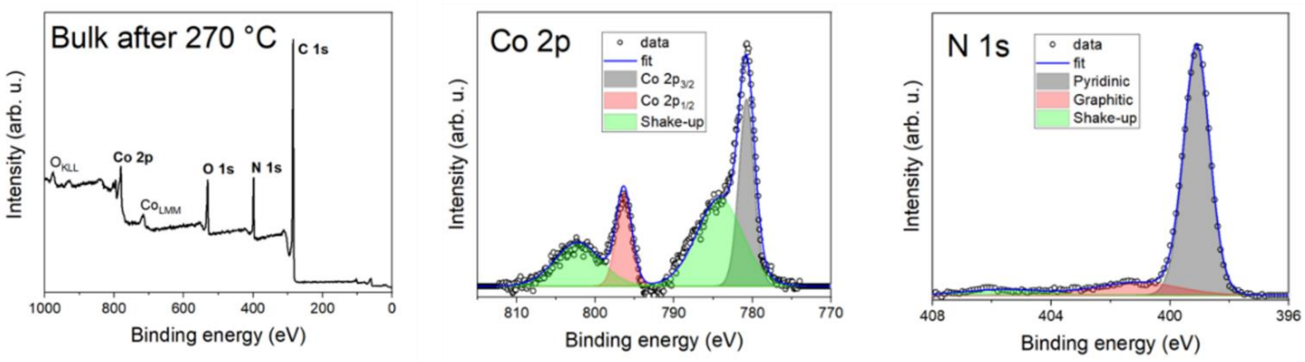

Fig. S11 Survey and detailed XPS spectra of bulk compound after sublimation at 270 °C for Co 2p and N 1s.

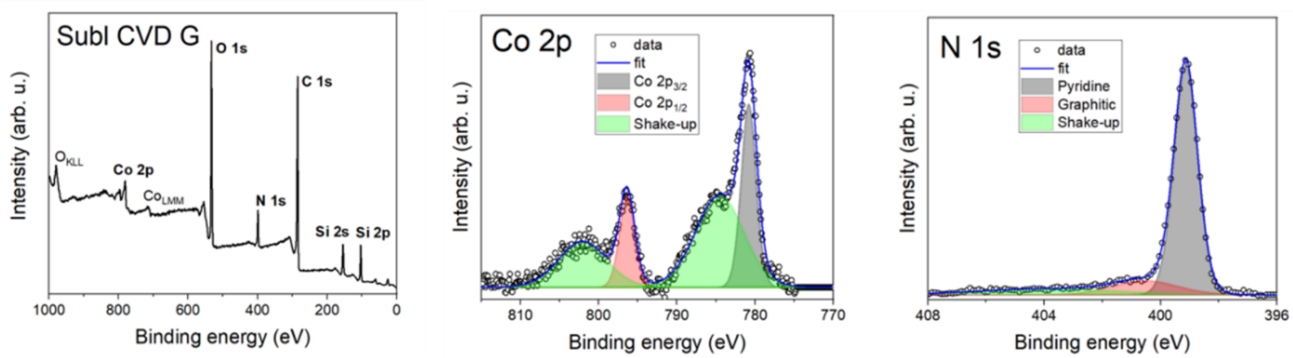

Fig. S12 Survey and detailed XPS spectra of deposited sample by thermal sublimation on CVD graphene for Co 2p and N 1s.

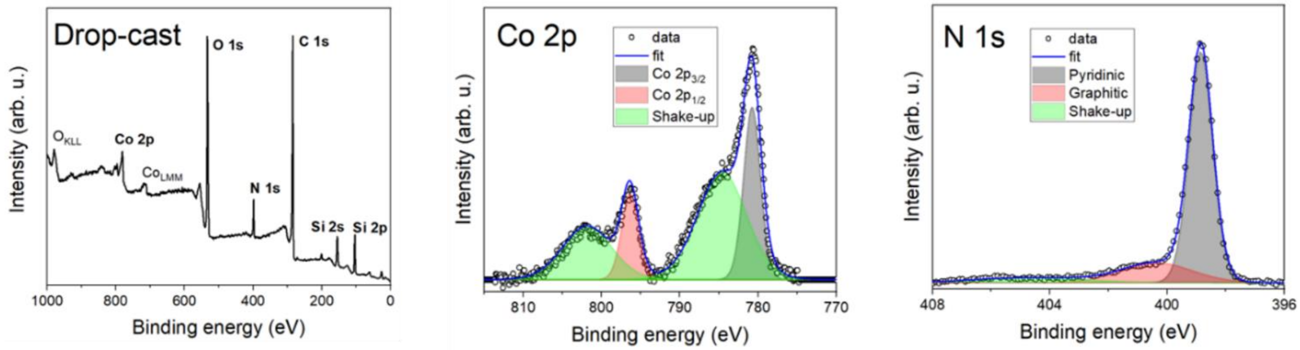

Fig. S13 Survey and detailed XPS spectra of deposited sample by drop-cast on CVD graphene for Co 2p and N 1s.

Elemental composition of the samples was evaluated using a semi-empirical approach. The integrated intensity of each component was corrected with the photoionization cross-section calculated for each atom, neglecting the differences in photoelectron escape length as a function of the kinetic energy [21]. The semi-quantitative analysis (see Table S5) showed that the ratio of Co:N / 1:4 in molecule remains preserved for all samples. Adventitious contributions from silicon wafer under graphene along with carbon and oxygen impurities hinders further quantitative analysis for deposited samples. Since hydrogen is not directly detected by XPS, it was neglected in the calculation of the atomic percentage.

Table S5 Comparison of the elemental composition of compound **1** determined by XPS for bulk, bulk after 270 °C, sublimation on CVD graphene, and drop-cast on CVD graphene

	Measured (%)			
Element	**Co (1)**	**N (4)**	**C (26)**	**O (2)**
Percentage for: $C_{26}H_{22}CoN_4O_2$	3	12.1	78.8	6.1
Bulk	2.7	11.7	79.7	5.9
Bulk after 270 °C	2.0	10.0	81.4	6.6
Sublimation	1.5	6.9	66.1	25.5
Drop-cast	1.9	6.3	67.1	24.7

Section S4. Analysis of Raman spectroscopy, XPS, and AFM of compound 2 in bulk and deposited on graphene

Deposition of compound **2**

To test the stability of compound **2** during deposition at ambient conditions, it was deposited by drop-casting. The bulk was dissolved in acetone (C_3H_6O, 99%, Penta, Czech Republic) to make a final solution with a 1 mM concentration. The actual drop-casting was conducted in ambient conditions as 40 μL was drop-cast onto a substrate. To test its thermal stability, deposition by thermal sublimation at pressure in the order of 10^{-7} mbar at 283 °C was performed. Thermal sublimation process took 137 hours. Optical images of the resulting samples can be seen in Figs. S14 (a,d).

The topography of both samples was investigated by AFM. As can be seen in Fig. S14, drop-cast led to the formation of crystals a few micrometers high, while thermal sublimation led to the formation of flaky islands several micrometers in size and up to 100 nm in height. The difference may be due to a different amount of deposited material.

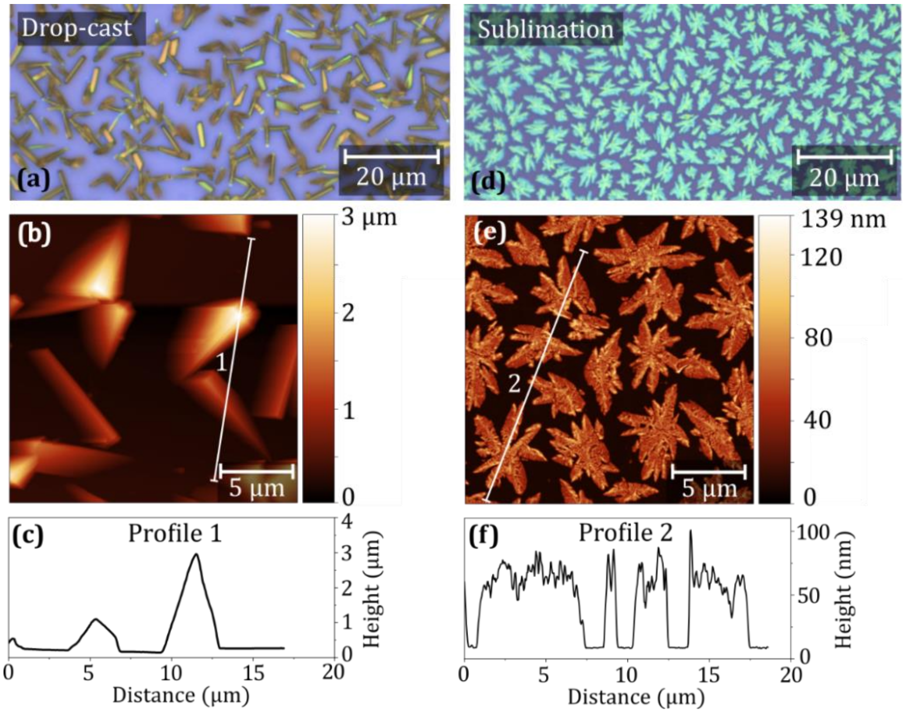

Fig. S14 Optical images of deposited compound **2** on CVD graphene by drop-cast (a) and thermal sublimation (d) with their AFM images (b) and (e), respectively. Height profiles (c) and (f) are along the white line indicated in the AFM images.

Raman Spectroscopy on Deposited Compound 2

Raman spectroscopy was performed to compare the vibrational modes of the individual components of the resulting hybrid material. Fig. S15 shows Raman spectra, from top to bottom, of a SiO_2/Si + CVD graphene, powder of the compound **2**, deposited compound **2** on graphene by drop-casting, and by thermal sublimation. The Raman spectrum of bulk compound **2** contained peaks characteristic of the ligand's functional groups such as imino or aromatic C=C/N bonds (ca. 1400–1620 cm^{-1}) or the phenolic group (1200–1300 cm^{-1}) [16]. We chose to use the following most intense peaks for comparison between the bulk and deposited materials (in cm^{-1}): 1226, 1349, 1421, 1561 and 1603. As can be seen from Fig. S15**,** Raman spectra of hybrid materials prepared either by wet or sublimation techniques confirmed the presence of all the peaks observed in the bulk material, and all the spectral patterns agree exceptionally well.

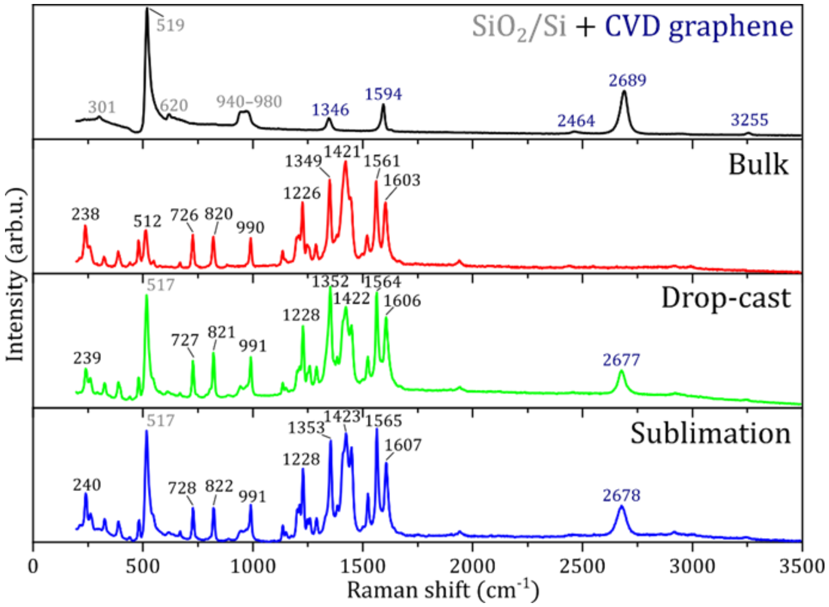

Fig. S15 Comparison of Raman spectra of the compound **2**, from top to bottom, of Si/SiO$_2$ substrate (Raman shift values marked in grey) and CVD graphene (marked in dark blue), bulk, and deposited by drop-cast and by thermal sublimation.

Table S6 Comparison of Raman shift peaks (in cm^{-1}) of Si/SiO$_2$ substrate and CVD graphene, bulk, deposited by drop-cast and by thermal sublimation. Peak intensity is denoted as follows: strong - s, medium - m, weak - w, very weak – vw

SiO$_2$ + CVD graphene	Bulk 2	Drop-cast on CVD graphene	Sublimation on CVD graphene
	236m	239m	239m
	257w	259w	262w
301w			
	322w	325w	325w
	387w	387w	387w
	441vw	441vw	441vw
	480m	482m	482w
519s	513m	516s	516s
	549vw	544vw	
620w		610vw	615vw
	670vw	670vw	670vw
	727m	727m	727m
	821m	821m	821m
	882vw	888vw	893vw
			914vw
940-980m		940-980vw	940-980w
	990m	990m	990m
			1029vw

	1089vw		
	1136m	1136w	1136w
	1146vw	1149vw	1154vw
	1200m	1203m	1203m
	1210m	1213m	1213m
	1226s	1228m	1228s
	1246m		1248w
		1258m	1258w
	1286m	1289m	1289w
1346m	1349s	1352s	1354s
	1382m	1384m	1384m
	1421s	1424s	1424s
	1444s	1446s	1449s
	1520m	1523m	1523m
	1562s	1564s	1564s
1594m			
	1603s	1603s	1606s
	1666vw	1671vw	1614m
1622vw			
	1892vw		1903vw
	1939w	1941w	1941w
	2446vw	2454vw	2452vw
2464vw			
	2547vw	2545vw	2552vw
2689m		2675m	2678m
	2913vw	2921vw	2919vw
2950vw			
	2988vw	3002vw	2998vw
3255vw		3248vw	3246vw

X-ray Photoelectron Spectroscopy (XPS)

The chemical composition was probed by XPS. Fig. S16 shows the comparison of XPS spectra for bulk and sublimated samples. All survey spectra exhibited the photoelectron peaks: Co 2p, N 1s, C 1s, and O 1s; and Auger peaks: O_{KLL} and Co_{LMM}.

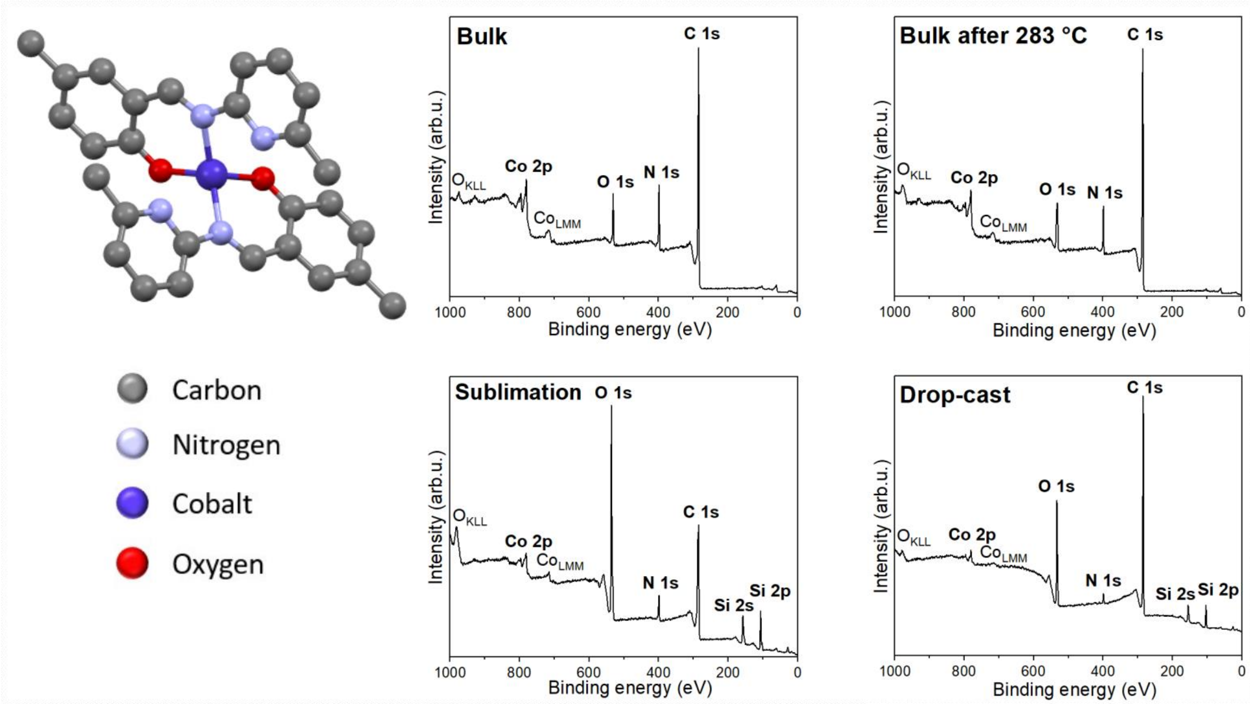

Fig. S16 Compound **2** with XPS survey comparison for bulk, bulk after 283 °C, sublimation on CVD graphene, and drop-cast on CVD graphene.

Both Co 2p peaks exhibited two main components Co 2p$_{3/2}$ and Co 2p$_{1/2}$ and shake-up satellites. The spin-orbit shift of the main components Co 2p$_{3/2}$ and Co 2p$_{1/2,}$ $\Delta = 15.5$ eV, corresponds to Co(II) in the high-spin state [22]. Satellites intensity slightly increased after sublimation. In the case of N 1s, the peak is deconvoluted into 3 components: at 399.1 eV – corresponding to pyridinic nitrogen in the ligand [23], the smallest peak at 405.7 eV may be attributed to a shake-up satellite [24]. Small peak at ~401 eV may correspond to a graphitic nitrogen [20]. In contrast to compound **1,** in the case of the sublimated and bulk after sublimation samples of compound **2**, an unidentified small peak appears at 399.9 eV. Detailed spectra of O 1s and C 1s are not shown since they are affected by adventitious contaminations due to the ex-situ preparation procedures.

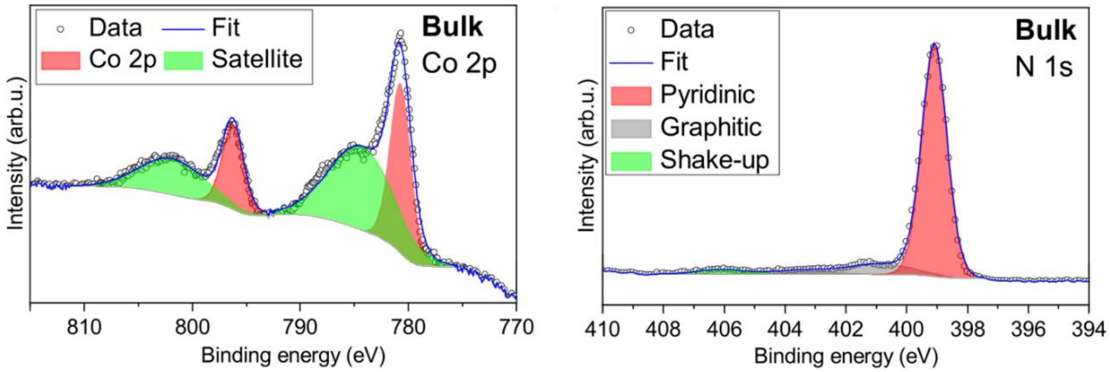

Fig. S17 Detailed XPS spectra of bulk compound **2** for Co 2p and N 1s.

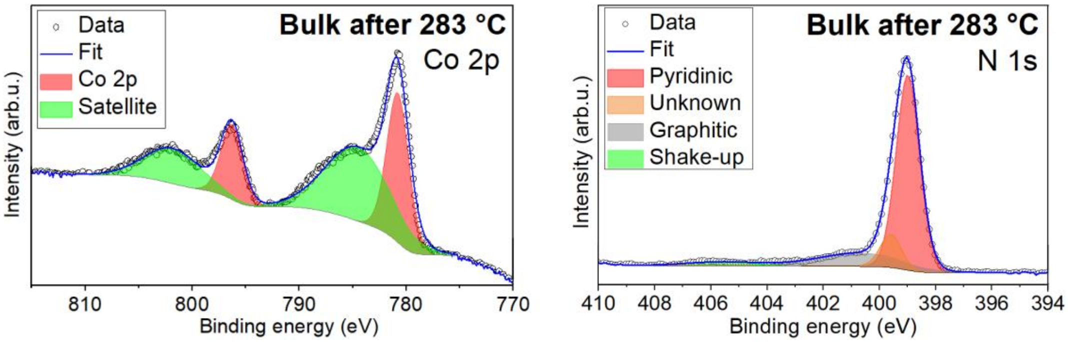

Fig. S18 Detailed XPS spectra of bulk compound **2** after sublimation at 283 °C for Co 2p and N 1s.

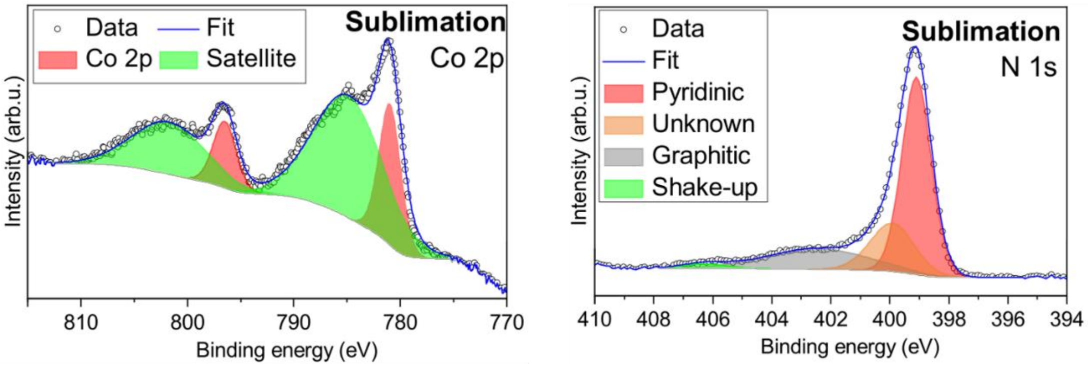

Fig. S19 Detailed XPS spectra of deposited sample by thermal sublimation on CVD graphene for Co 2p and N 1s.

In the case of the drop-cast depositions, it was impossible to compare the spectra because we found possible X-ray induced damage or partial charging of the sample during the measurements. This is shown in Fig. S20 of the detailed nitrogen spectrum, where on the left – the peak after 2 scans is composed of two components, while on the right – after 25 scans, another component appears.

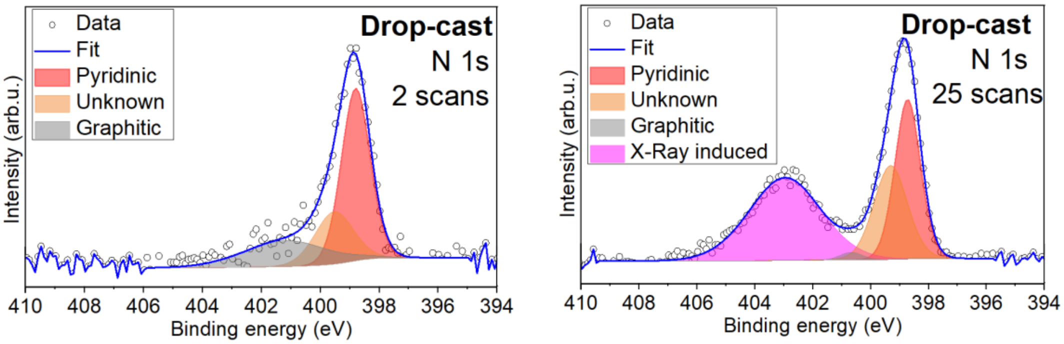

Fig. S20 Comparison of XPS spectra of the compound **2** drop-casted on graphene depending on the number of scans.

The following Table S7 shows the semi-quantitative analysis of elemental composition. The analysis showed that the ratio of Co:N / 1:4 in molecule remains preserved for all samples. Adventitious contributions from silicon wafer under graphene along with carbon and oxygen impurities hinders further quantitative analysis for deposited samples. Since hydrogen is not directly detected by XPS, it was neglected in the calculation of the atomic percentage.

No analysis was performed for the drop-cast for the reason mentioned above.

Table S7 Comparison of the elemental composition of compound **2** determined by XPS for bulk, bulk after 283 °C, and sublimation on CVD graphene

	Measured (%)			
Element	**Co (1)**	**N (4)**	**C (28)**	**O (2)**
Percentage for: $C_{28}H_{26}CoN_4O_2$	2.9	11.4	80.0	5.7
Bulk	2.3	10.5	82.1	5.0
Bulk after 283 °C	1.82	8.4	82.0	7.7
Sublimation	1.4	5.4	63.9	29.3

S5. Results of Magnetic Exchange Interaction and Zero-Field Splitting Terms by BS-DFT and CASSCF-NEVPT2

Table S8. Evaluation of the magnetic exchange by the broken-symmetry DFT approach for **1**. The definitions of each term of the table are found in the main text

Functional	Basis	$\langle S_{HS}^2 \rangle$	$\langle S_{BS}^2 \rangle$	Δ (cm^{-1})	J^R (cm^{-1})	J^Y (cm^{-1})
B3LYP+NL	def2-TZVP	12.0246	3.0246	-1.110	-0.185	-0.247
B3LYP+NL	ZORA-def2-TZVP	12.0264	3.0263	-1.066	-0.178	-0.237
B3LYP+SCNL	ZORA-def2-TZVP	12.0274	3.0273	-1.093	-0.182	-0.243
PBE0+NL	def2-TZVP	12.0231	3.0231	-0.781	-0.130	-0.174
PBE0+NL	ZORA-def2-TZVP	12.0247	3.0247	-0.766	-0.128	-0.170
PBE0+SCNL	ZORA-def2-TZVP	12.0253	3.0253	-0.762	-0.127	-0.169

Table S9. Evaluation of the magnetic exchange by the broken-symmetry DFT approach for **2**

Functional	Basis	$\langle S_{HS}^2 \rangle$	$\langle S_{BS}^2 \rangle$	Δ (cm^{-1})	J^R (cm^{-1})	J^Y (cm^{-1})
B3LYP+NL	def2-TZVP	12.0257	3.0257	-1.206	-0.201	-0.268
B3LYP+NL	ZORA-def2-TZVP	12.0276	3.0276	-1.216	-0.203	-0.270
B3LYP+SCNL	ZORA-def2-TZVP	12.0287	3.0287	-1.205	-0.201	-0.268
PBE0+NL	def2-TZVP	12.0241	3.0241	-0.906	-0.151	-0.201
PBE0+NL	ZORA-def2-TZVP	12.0258	3.0258	-0.892	-0.149	-0.198
PBE0+SCNL	ZORA-def2-TZVP	12.0264	3.0264	-0.890	-0.148	-0.198

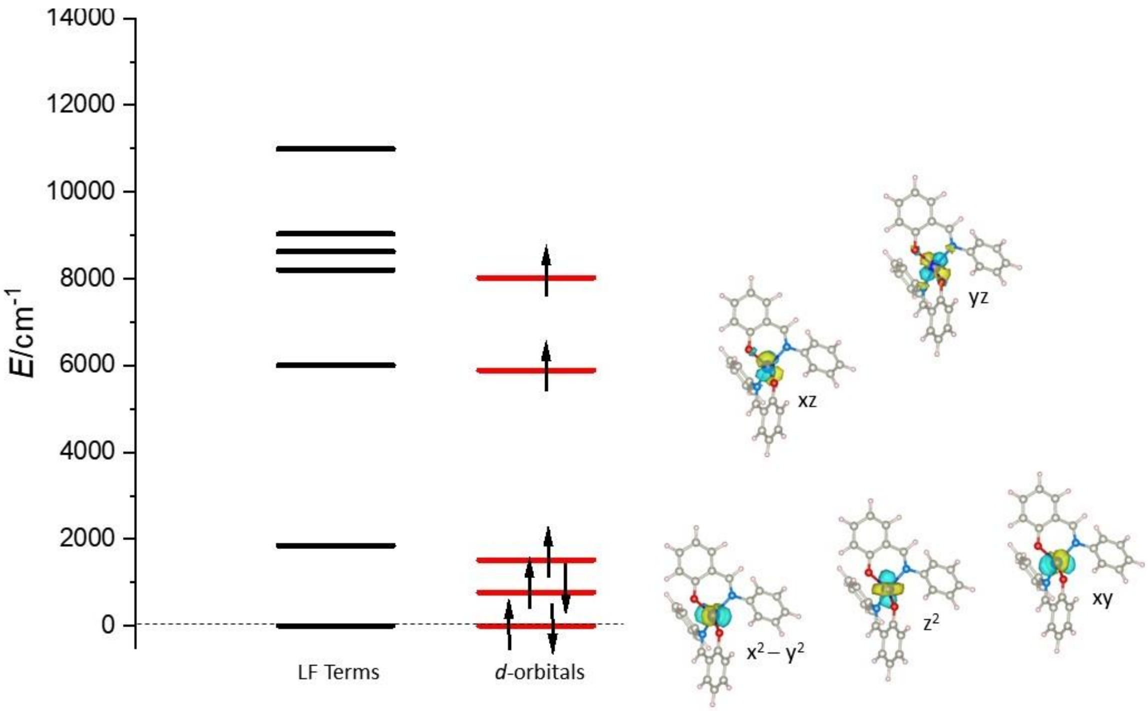

Fig. S21 CASSCF-NEVTP2 (AILFT) calculated LF terms and *d*-orbital splitting for **1**.

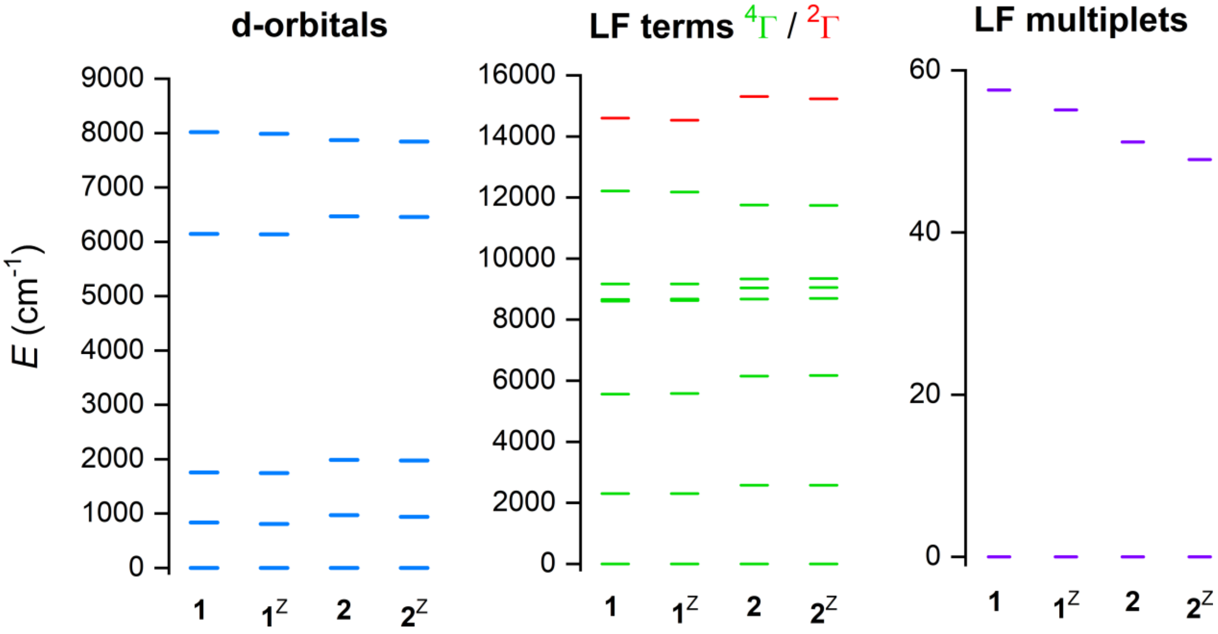

Fig. S22 CASSCF-NEVPT2 calculations for **1** and **2**. The calculations with scalar relativistic corrections ZORA are labelled as $\mathbf{1}^{Z}$ and $\mathbf{2}^{Z}$. (left) AILFT *d*-orbitals, (middle) ligand field terms, and (right) ligand field multiplets showing the zero-field splitting of two lowest Kramers doublets.

Table S10 Evaluation of the zero-field splitting parameters by CASSCF-NEVPT2 for **1** and **2**

Compound, basis	D (cm^{-1})	E/D	g_x	g_y	g_z	$U_{1\text{-}2}$ (cm^{-1})
1, def2-TZVP	-25.3	0.084	2.185	2.126	2.462	51.16
1, ZORA-def2-TZVP	-24.2	0.084	2.181	2.123	2.453	48.99
2, def2-TZVP	-28.3	0.107	2.201	2.119	2.501	57.58
2, ZORA-def2-TZVP	-27.1	0.107	2.197	2.117	2.491	55.13

Table S11. Evaluation of the *g*-factors for $S_{\mathrm{eff}} = 1/2$ for the ground Kramers doublet by CASSCF-NEVPT2 for **1** and **2**

Compound, basis	g_1	g_2	g_3	$\mathrm{g}_{\mathrm{iso}}$
1, def2-TZVP	0.512	0.568	7.323	2.801
1, ZORA-def2-TZVP	0.509	0.565	7.297	2.790
2, def2-TZVP	0.637	0.731	7.405	2.924
2, ZORA-def2-TZVP	0.633	0.726	7.377	2.912

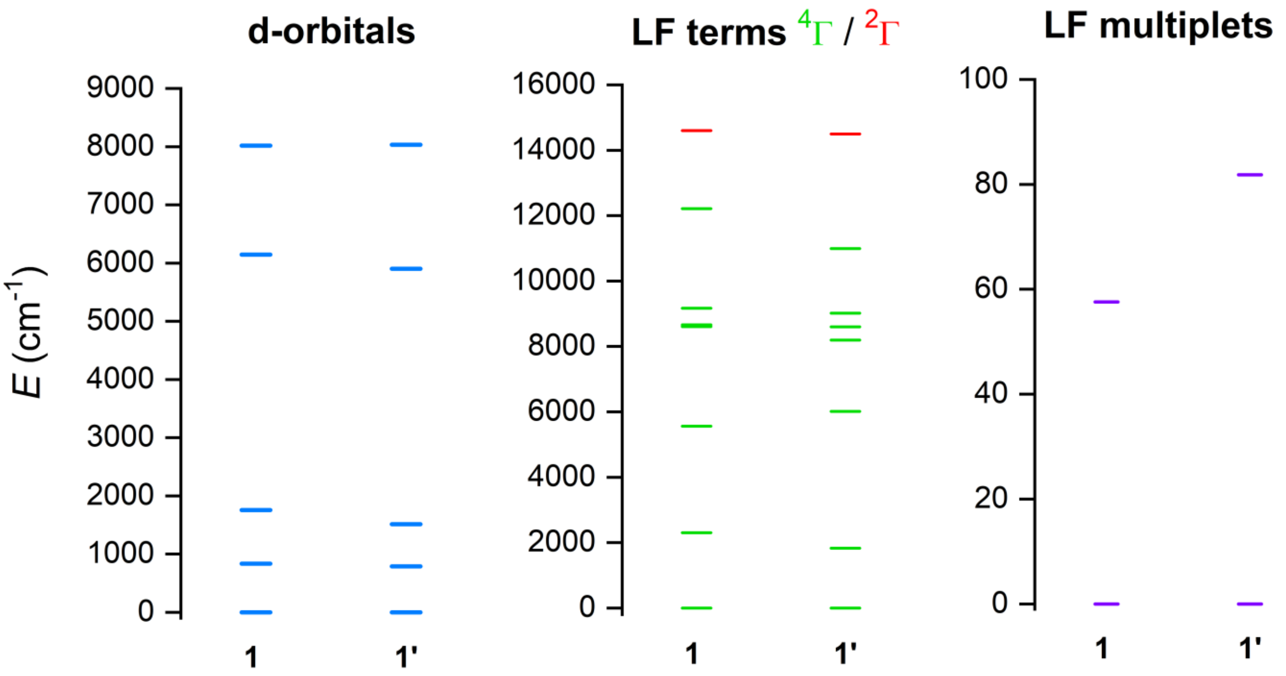

Fig. S23 CASSCF-NEVPT2 calculations for **1** and **1'**. (Left) AILFT *d*-orbitals, (middle) ligand field terms, and (right) ligand field multiplets showing the zero-field splitting of two lowest Kramers doublets

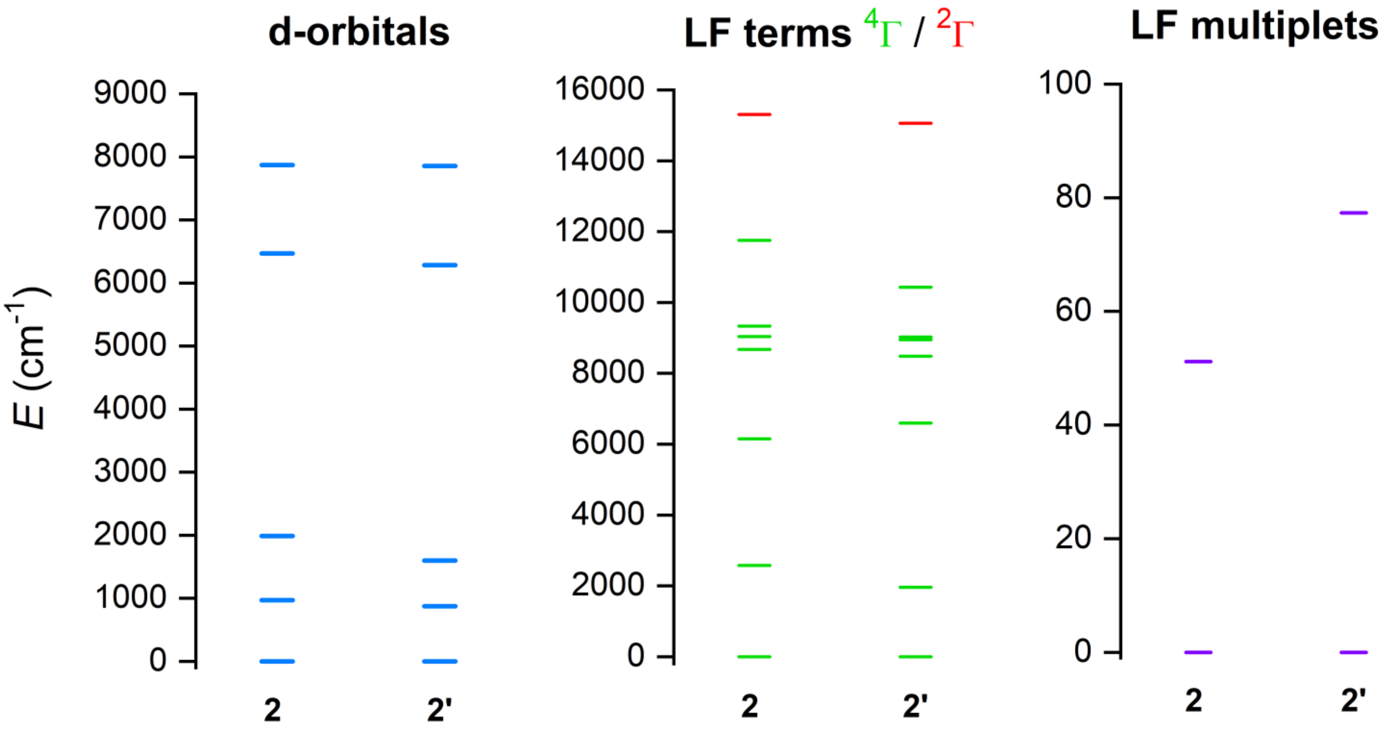

Fig. S24 CASSCF-NEVPT2 calculations for **2** and **2'**. (Left) AILFT *d*-orbitals, (middle) ligand field terms, and (right) ligand field multiplets showing the zero-field splitting of two lowest Kramers doublets

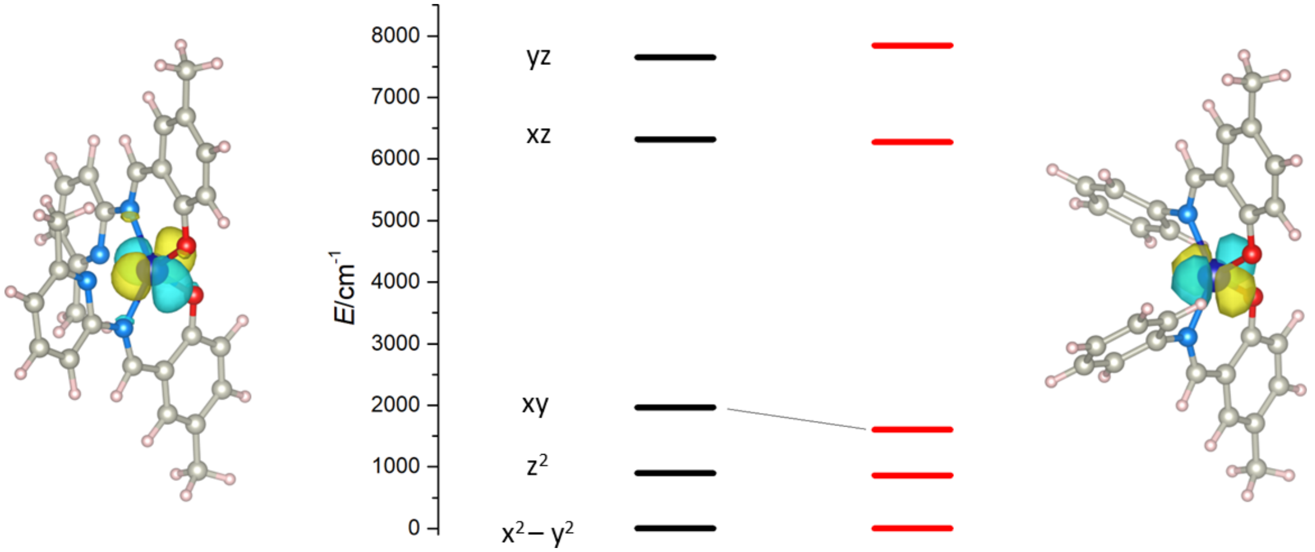

Fig. S25 The orbital splitting resulting from the AILFT (NEVPT2) calculations is shown for molecular structures **2** (left) and **2'** (right). The d-orbitals are represented as black bars for **2** and red bars for **2'**. The decrease in d_{xy} energy is highlighted by the black line.

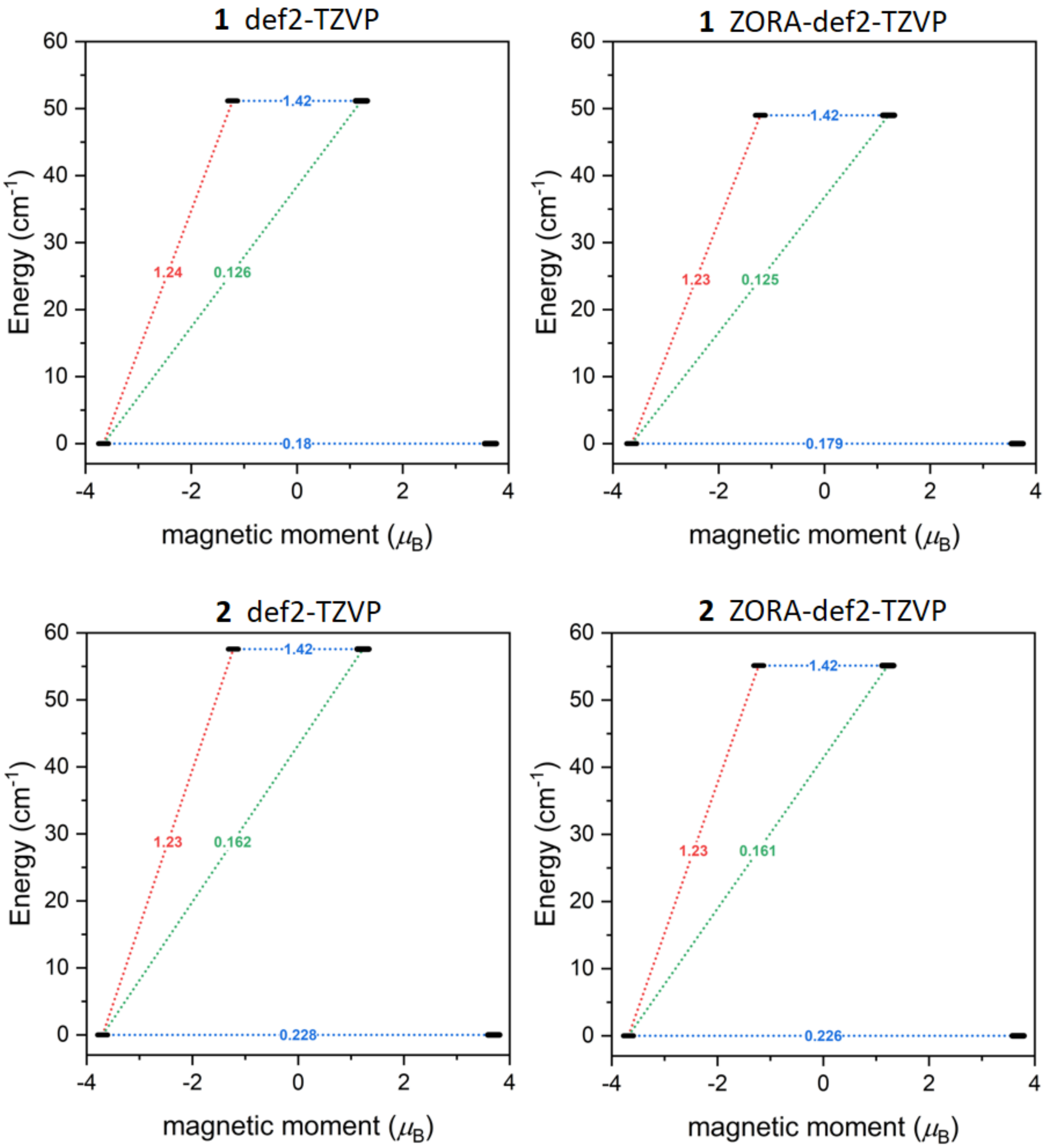

Fig. S26 Outcome of SINGLE_ANISO CASSCF-NEVPT2 calculations for **1** and **2**, considering different DFT basis sets. The numbers presented in the plots represent the corresponding matrix element of the transversal magnetic moment (for values larger than 0.1, an efficient relaxation mechanism is expected). Dashed lines refer to (temperature-assisted) quantum tunneling (QT) (blue), Orbach/Raman mechanisms (red), and direct/Raman mechanisms (green).

S6. DC Magnetization and HF-ESR Measurements

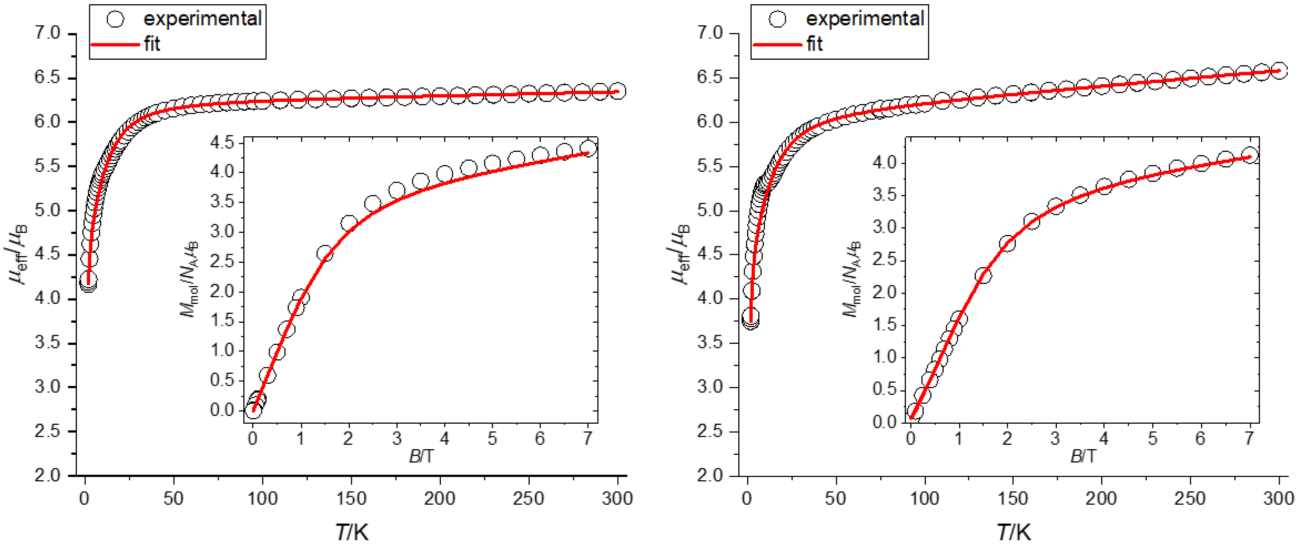

Fig. S27 Temperature (2-300K) and field dependence (in inset, 0-7T, at 2K) of magnetic data measured for complex **1** (left) and **2** (right). The experimental data (black circles) were fitted (red line) using Eq. 2 of the main text. The fit resulted in the following set of parameters, for compound **1**: g_{iso} = 2.272, D = -15.30 cm^{-1}, χ_{tip} = 8.245×10^{-9}, J = -0.192 cm^{-1}, E/D = 0.012; for compound **2**: g$_{iso}$ = 2.213, D = -17.47 cm^{-1}, χ_{tip} = 3.489×10^{-8}, J = -0.265 cm^{-1}, E/D = 0.044.

Below, Fig. S28 shows the temperature dependence of the HF-ESR signal at different frequencies, and the simulated spectra with parameters S = 3/2, g_x = 2.20, g_y = 2.15, g_z = 2.40, D = -20 cm^{-1}, E/D = 0.122, and J = -0.3 cm^{-1}. The red dot, green star and black cross have the same meaning as in the main text. Fig. S29 shows levels plot of the spin system in different spin orientations.

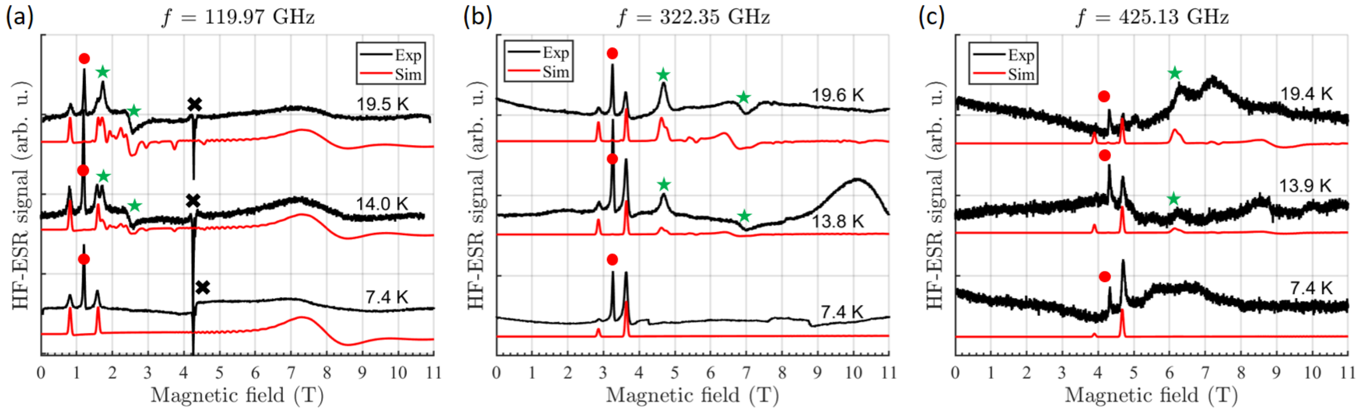

Fig. S28 Temperature dependence of the HF-ESR measurements at frequencies (a) f = 119.97 GHz, (b) f = 322.35 GHz, and (c) f = 425.13 GHz.

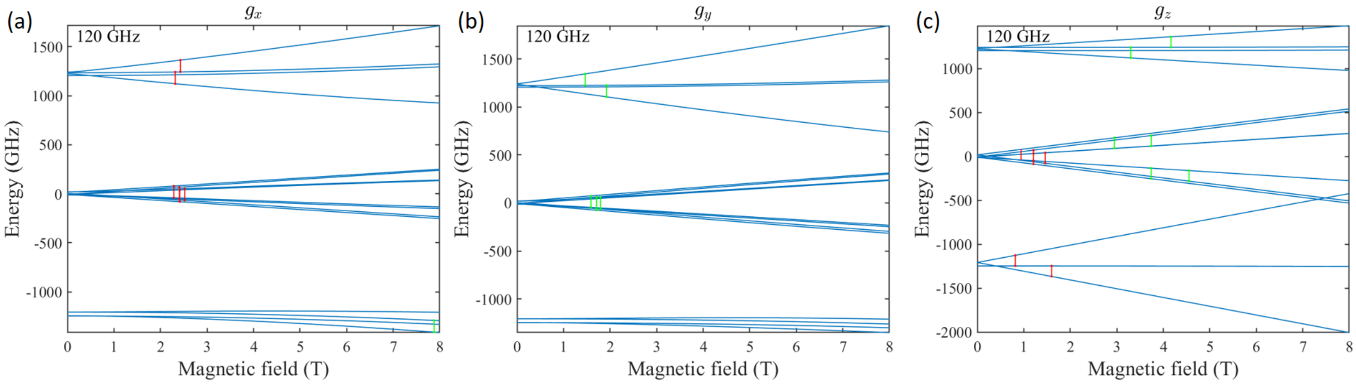

Fig. S29 Levels plot of the spin system with parameters $S = 3/2$, $g_x = 2.20$, $g_y = 2.15$, $g_z = 2.40$, $D = -20$ cm^{-1}, $E/D = 0.122$, and $J = -0.3$ cm^{-1}, for different spin components. The red and green lines correspond to electric dipole forbidden and allowed ESR transitions at $f = 120$ GHz. Electric dipole forbidden transitions are nonetheless visible in ESR spectra with a lower intensity.

Fig. S30 displays the HF-ESR measurements of the bulk compared to deposited samples of compound **1** on graphene, by drop-cast and sublimation. Clear sharp peaks indicated with an asterisk correspond to the ESR response with *g*-factor 2 due to impurities in the mirror/substrate/sample and are not related to the Co(II) center in **1**. Sharp features similar to the bulk powder sample around 2 T in (a) and 3.5 T in (b) are not observed in the deposited samples. On the other hand, very small and broad features in the level of the noise in the deposited samples are spread within the measured spectra. Indeed, a preferential orientation upon deposition would result in resonances at different magnetic field compared to the powder sample. However, we do not have enough sensitivity to confirm this possibility unequivocally.

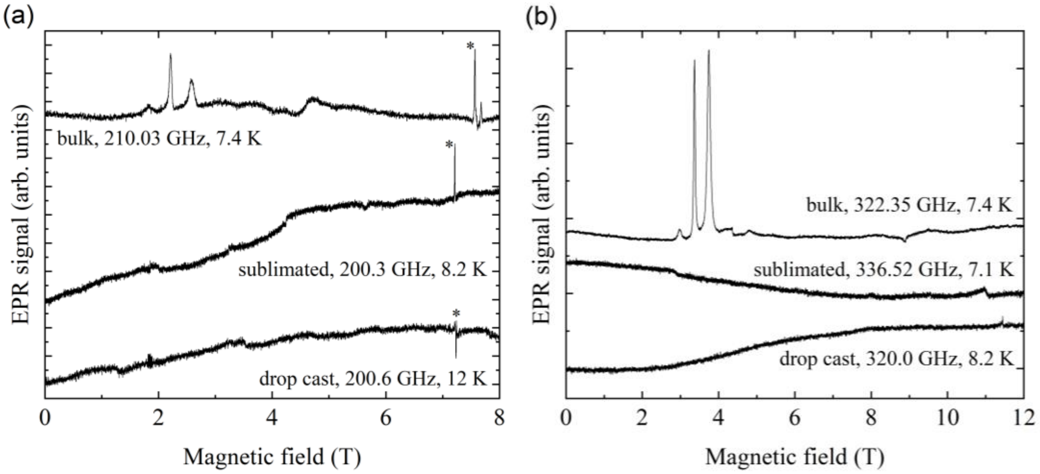

Fig. S30 Comparison of HF-ESR spectra of compound **1** in bulk state (powder spectra) and deposited on graphene by drop-cast and thermal sublimation, at frequencies around (a) 200 GHz and (b) 320 GHz.

S7. Dynamic magnetic investigations

The magnetic data induced by an oscillating, alternating-current (AC) magnetic field were recorded for both complexes **1** and **2** at zero as well as at applied static DC field. At 2 K, no signal of out-of-phase susceptibility (χ'') was observed at zero DC field, which indicates the relaxation of magnetization mediated via quantum tunneling (QT) effect. The applied DC field, however, caused the evolution of an out-of-phase susceptibility. To determine the optimum DC field to suppress the QT of magnetization, AC susceptibility under various DC fields was measured at 2 K. Collected sets of in-phase χ' and out-of-phase χ'' components of AC susceptibility (20 χ' and 20 χ'') at each DC field were fitted using the formulas for the extended one-set Debye model:

$$\chi'(\omega) = \chi_S + (\chi_T - \chi_S)\frac{1 + (\omega\tau)^{1-\alpha}\sin(\pi\alpha/2)}{1 + 2(\omega\tau)^{1-\alpha}\sin(\pi\alpha/2) + (\omega\tau)^{2-2\alpha}}, \tag{S1}$$

$$\chi''(\omega) = (\chi_T - \chi_S)\frac{(\omega\tau)^{1-\alpha}\sin(\pi\alpha/2)}{1 + 2(\omega\tau)^{1-\alpha}\sin(\pi\alpha/2) + (\omega\tau)^{2-2\alpha}}. \tag{S2}$$

Table S12 Conditions of AC magnetic experiments for compound **1**

B_{DC} (T)	***T* (K)**	**Frequency range**
0 – 0.15	2	10-1000 Hz (10 steps)
0.06	1.9 - 4.9	0.1-1000 Hz (20 steps)
0.08	1.9 - 4.9	0.1-1000 Hz (20 steps)

Table S13 Parameters of the extended one-set Debye model (Eqs. S1 and S2) for compound **1** measured from 0 T to 1 T at *T* = 2.0 K

***B* (T)**	**χ_T (10^{-6} cm^3 mol^{-1})**	**χ_S (10^{-6} cm^3 mol^{-1})**	**α (10^{-2})**	**τ (10^{-3} s)**	**R^2**
0	-	-	-	-	-
0.005	-	-	-	-	-
0.01	7.25(1)	6.43(2)	0.27(3)	0.69(4)	0.99996
0.015	7.33(2)	5.43(3)	0.26(2)	0.90(3)	0.99983
0.02	7.39(3)	4.51(4)	0.24(2)	1.16(3)	0.99957
0.03	7.44(4)	3.20(4)	0.19(1)	1.68(4)	0.99899
0.04	7.44(4)	2.41(3)	0.15(1)	2.07(3)	0.99889
0.05	7.42(4)	1.91(2)	0.135(7)	2.29(3)	0.99897
0.06	7.41(3)	1.58(2)	0.126(6)	2.37(2)	0.99919
0.07	7.39(3)	1.34(2)	0.122(5)	2.33(2)	0.99942
0.08	7.36(2)	1.17(2)	0.121(4)	2.12(1)	0.99954
0.09	7.35(2)	1.03(2)	0.129(4)	1.76(1)	0.99954
0.1	7.33(2)	0.94(2)	0.138(5)	1.34(1)	0.99954
0.125	7.31(3)	0.88(7)	0.241(9)	0.41(9)	0.99937
0.15	7.18(2)	2.5(2)	0.27(2)	0.2(2)	0.99977

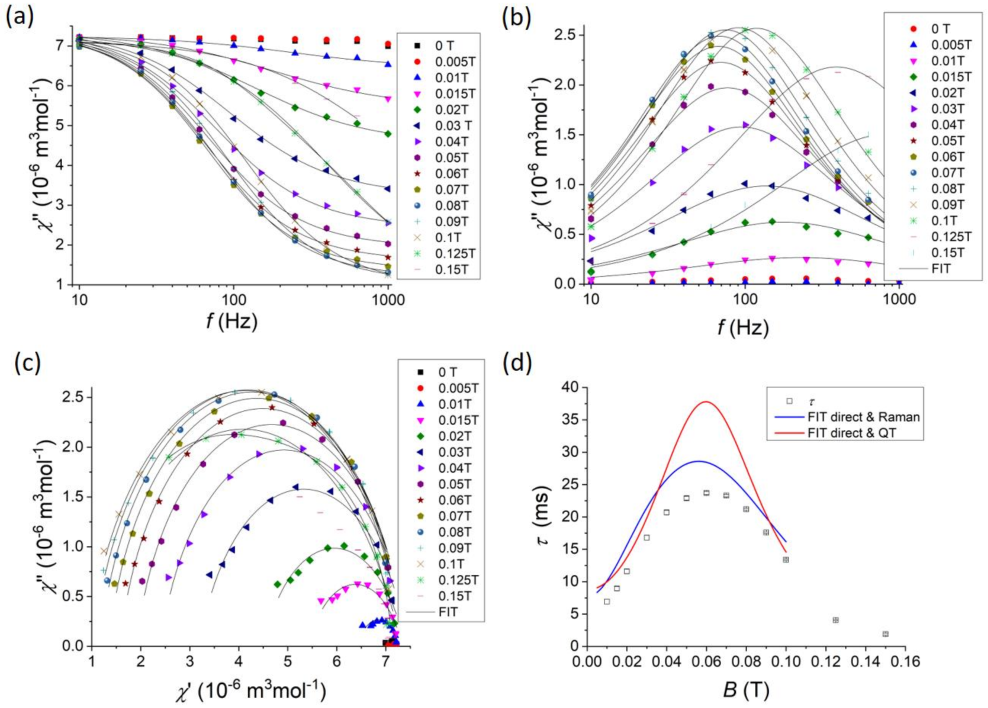

Fig. S31 AC susceptibility data for **1** recorded at various static magnetic fields at T = 2.0 K: Frequency dependent in-phase χ'(a) and out-of-phase χ''(b) component of AC susceptibility and Cole-Cole diagram (c) (solid lines are results of fits according to equations S1 and S2). (d) Field dependency of relaxation time τ (solid lines are fits to the combination of direct and Raman processes or to the combination of direct process and QT).

Table S14 Parameters of the extended one-set Debye model (Eqs. S1 and S2) for **1** measured in the temperature range 1.9-4.9 K at 0.06 T

T (K)	χ_T (10^{-6} cm^3 mol^{-1}-)	χ_S (10^{-6} cm^3 mol^{-1})	α (10^{-2})	τ (10^{-3} s)	R^2
1.9	9.08(2)	2.07(3)	0.096(6)	2.26(2)	0.9994
2.1	8.63(1)	1.93(2)	0.098(4)	2.20(2)	0.99968
2.3	8.22(1)	1.83(2)	0.096(4)	2.12 (2)	0.99968
2.5	7.83(1)	1.73(2)	0.094(4)	2.01(2)	0.99971
2.7	7.471(9)	1.65(2)	0.093(3)	1.88(2)	0.99972
2.9	7.13(1)	1.58(2)	0.087(5)	1.73(2)	0.99958
3.1	6.854(7)	1.51(2)	0.085(3)	1.5(1)	0.99958
3.3	6.569(6)	1.45(2)	0.075(3)	1.29(8)	0.99982
3.5	6.319(5)	1.39(2)	0.063(3)	1.39(2)	0.99985
3.7	6.076(3)	1.35(1)	0.046(2)	0.65(2)	0.99993
3.9	5.86(3)	1.30(1)	0.032(2)	0.34(2)	0.99995
4.1	5.65(3)	1.30(2)	0.021(3)	0.22(2)	0.99994
4.3	5.47(2)	1.39(4)	0.011(4)	0.13(2)	0.99996
4.5	5.290(2)	1.68(3)	0	0.083(8)	0.99997
4.7	5.134(2)	2.18(6)	0	0.057(2)	0.99997
4.9	4.980(2)	2.94(2)	0	0.049(3)	0.99995

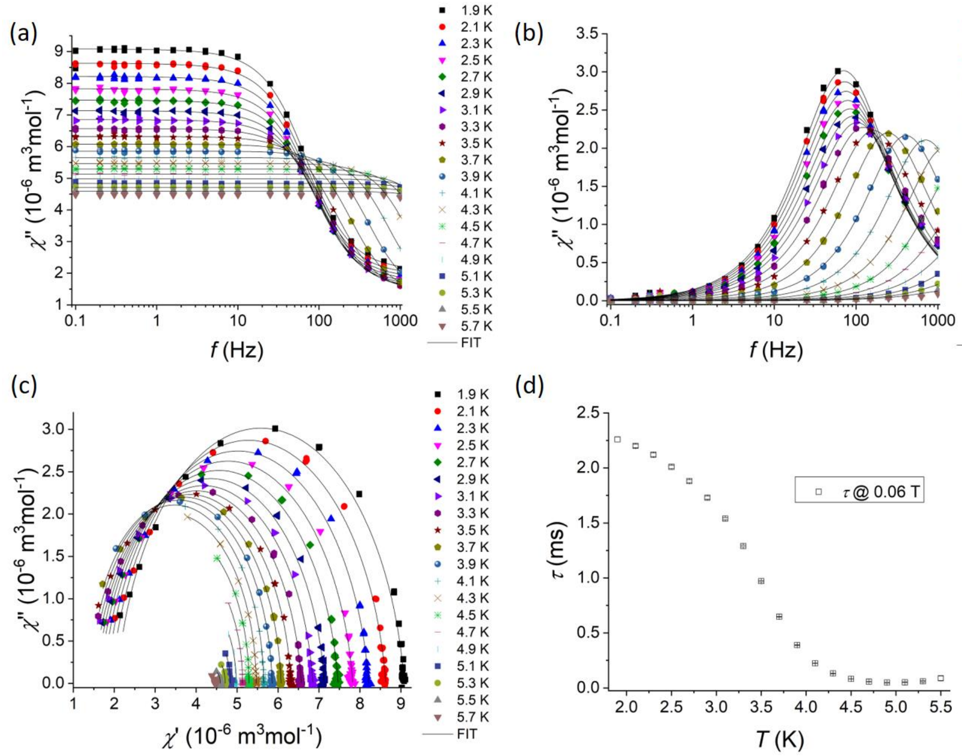

Fig. S32 AC susceptibility data for **1** recorded at various temperatures at 0.06 T: Frequency dependent in-phase χ'(*a*) and out-of-phase χ''(b) component of AC susceptibility and Cole-Cole diagram (c) (solid lines are results of fits according to Eqs. S1 and S2). (d) Field dependency of relaxation time τ.

Table S15 Parameters of the extended one-set Debye model (Eqs. S1 and S2) for **1** measured at 0.08 T

***T* (K)**	**χ_T (10^{-6} cm^3 mol^{-1})**	**χ_S (10^{-6} cm^3 mol^{-1})**	**α (10^{-2})**	**τ (10^{-3} s)**	**R^2**
1.9	7.39(1)	1.27(2)	0.098(5)	2.07(1)	0.99955
2.1	7.02(1)	1.20(3)	0.099(6)	2.03(2)	0.99932
2.3	6.71(1)	1.12(2)	0.102(4)	1.99(2)	0.9996
2.5	6.358(9)	1.08(2)	0.094(5)	1.9(2)	0.99959
2.7	6.10(2)	1.03(3)	0.098(9)	1.82(3)	0.99836
2.9	5.84(1)	0.98(2)	0.096(5)	1.71(2)	0.99944
3.1	5.59(1)	0.95(3)	0.088(7)	1.54(2)	0.99903
3.3	5.329(8)	0.93(2)	0.070(5)	1.29(1)	0.99959
3.5	5.139(5)	0.90(1)	0.058(4)	0.98(6)	0.99977
3.7	4.916(8)	0.88(3)	0.034(4)	0.65(7)	0.99937
3.9	4.761(7)	0.85(3)	0.028(6)	0.39(5)	0.99937
4.1	4.622(9)	0.83(8)	0.03(1)	0.23(6)	0.9991
4.3	4.429(9)	0.99(8)	0	0.13(4)	0.99907
4.5	4.302(5)	1.2(1)	0	0.084(4)	0.9997
4.7	4.176(5)	1.6(4)	0.01(2)	0.05(1)	0.99972
4.9	4.051(4)	2.3(4)	0	0.05(1)	0.99975

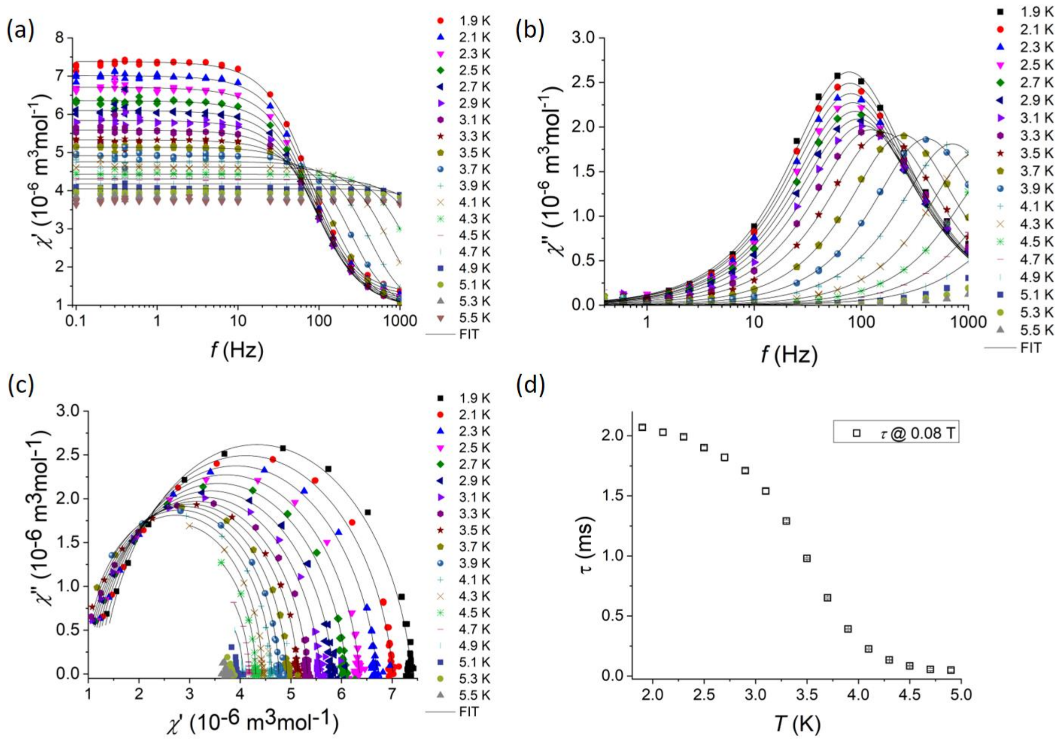

Fig. S33 AC susceptibility data for **1** recorded at various temperatures at 0.08 T: Frequency dependent in-phase χ'(a) and out-of-phase χ''(b) component of AC susceptibility and Cole-Cole diagram (c) (solid lines are results of fits according to equations S1 and S2). (d) Field dependency of relaxation time τ.

Table S16 Relaxation parameters for compound **1** obtained by fitting of τ vs B dependency at T = 2 K using the respective combinations of Raman, direct and QT relaxation processes

Model	**a (T^{-m} K^{-1} s^{-1})** **m**	**2^n*d (s^{-1})**	**e (K^{-2})** **f (K^{-2})**	**b_1 (s^{-1})** **b_2 (T^{-2})**	**R^2**
Direct & Raman[a]	1.8(6) × 10^6 4 (fixed)	1297(127)	757(513) 4113(1927)	-	0.88868
Direct & QT[a]	3.1(5) × 10^6 4 (fixed)	-	-	757(513) 4113(1927)	0.88868

[a] for fields in the range 0-0.1 T

Table S17 Relaxation parameters at B_{DC} = 0.06 T for compound **1** using the respective combinations relaxation processes

Model	**U/k_B (K)**	**τ_0 (s)**	**τ_{QTM}^{-1} (s^{-1})**	**aH^m (K^{-1} s^{-1})**	**R^2**
Orbach[a]	40(2)	1.2(5) × 10^{-8}	-	-	0.99097
Orbach + direct	53(2)	6(3) × 10^{-10}	-	203(5)	0.99756
Orbach & direct & QT	47(1)	2.6(9) × 10^{-9}	492(14)	8 × 10^{-22}	0.99702
Orbach & QT	47(1)	2.6(9) × 10^{-9}	492(13)	-	0.99727

[a] for data in the range 3.5 K - 4.7 K

Table S18 Relaxation parameters at B_{DC} = 0.08 T for compound **1** using the respective combinations relaxation processes

Model	**U/k_B (K)**	**τ_0 (s)**	**τ_{QTM}^{-1} (s^{-1})**	**aH^m (K^{-1} s^{-1})**	**R^2**
Orbach[a]	40(2)	$1.1(4) \times 10^{-8}$	-	-	0.99064
Orbach & direct	55(2)	$4(2) \times 10^{-10}$	-	213(6)	0.99602
Orbach & direct & QT	48(1)	$1.9(5) \times 10^{-8}$	521(10)	8×10^{-19}	0.99852
Orbach & QT	48(1)	$1.9(5) \times 10^{-8}$	521(9)	-	0.99864

[a] for data in the range 3.5 K - 4.7 K

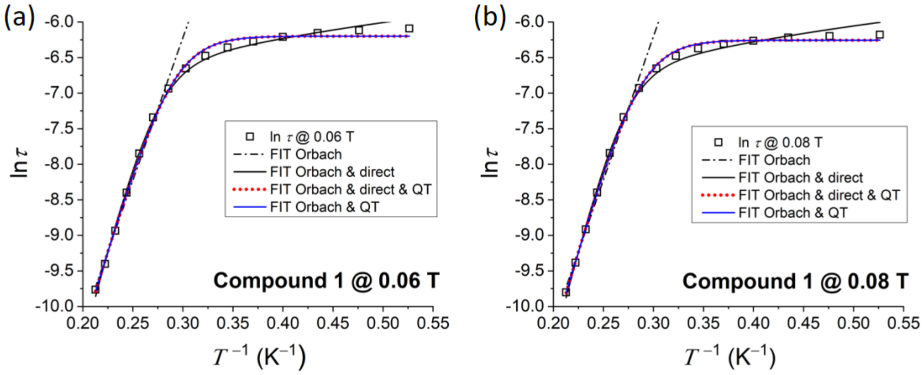

Fig. S34 ln τ vs 1/T dependencies fitted to the respective relaxation processes for **1** at two different static magnetic fields.

Table S19 Relaxation parameters of compound **1** obtained from the simultaneous fit of two ln τ vs 1/T dependencies recorded at 0.06 T and 0.08 T DC fields

Model	**U/k_B (K)**	**τ_0 (s)**	**τ_{QTM}^{-1} (s^{-1})**	**a (T^{-m} K^{-1} s^{-1}) m**	**R^2**
Orbach & QT	47.8(9)	$2.2(5) \times 10^{-9}$	506(8)	-	0.99788
Orbach & direct	48(7)	$2(4) \times 10^{-9}$	-	$a = 8(1) \times 10^{6}$ m = 4 (fixed)	0.87825
Orbach & direct & QT	48.2(8)	$2.0(4) \times 10^{-9}$	477(14)	$a = 4(2) \times 10^{5}$ m = 4 (fixed)	0.9982

Table S20 Conditions of AC magnetic experiments for compound **2**

B_{DC} (T)	**T (K)**	**Frequency range**
0 – 1	2	10-1000 Hz (10 steps)
0.09	1.9-4.1	0.1-1000 Hz (20 steps)
0.125	1.9-4.1	0.1-1000 Hz (20 steps)

Table S21 Parameters of the extended one-set Debye model (Eqs. S1 and S2) for **2** measured from 0 T to 1 T at T = 2.0 K

B (T)	χ_T (10^{-6} cm^3 mol^{-1})	χ_S (10^{-6} cm^3 mol^{-1})	α (10^{-2})	τ (10^{-3} s)	R^2
0	-	-	-	-	-
0.005	-	-	-	-	-
0.01	5.88(6)	5.41(1)	0.12(3)	0.49(5)	0.99996
0.015	5.901(6)	4.74(1)	0.14(1)	0.54(1)	0.99996
0.02	5.922(7)	4.06(1)	0.147(7)	0.624(8)	0.99995
0.03	5.95(1)	2.97(1)	0.139(5)	0.828(8)	0.99988
0.04	5.97(1)	2.27(1)	0.129(5)	1.030(8)	0.99988
0.05	5.98(1)	1.82(1)	0.123(4)	1.210(8)	0.99977
0.06	5.96(1)	1.52(1)	0.112(4)	1.350(9)	0.99971
0.07	5.96(1)	1.32(1)	0.107(4)	1.450(9)	0.99969
0.08	5.97(1)	1.17(1)	0.102(4)	1.51(1)	0.99964
0.09	5.95(2)	1.07(1)	0.095(4)	1.52(1)	0.99959
0.1	5.93(1)	0.99(1)	0.094(4)	1.500(9)	0.99959
0.125	5.91(2)	0.86(2)	0.100(4)	1.360(9)	0.99954
0.15	5.88(2)	0.88(3)	0.110(6)	0.88(9)	0.99928
0.2	5.83(2)	1.80(3)	0.15(1)	0.24(7)	0.9996
0.3	5.71(1)	3.74(9)	0.19(2)	0.16(1)	0.99981
0.4	5.64(2)	3.18(1)	0.23(3)	0.17(2)	0.99954
0.5	5.48(3)	3.10(3)	0.34(4)	0.13(3)	0.99932
0.75	5.1(1)	2.4(4)	0.50(7)	0.4(1)	0.99673
1	4.6(3)	1.6(5)	0.5(1)	0.5(3)	0.989

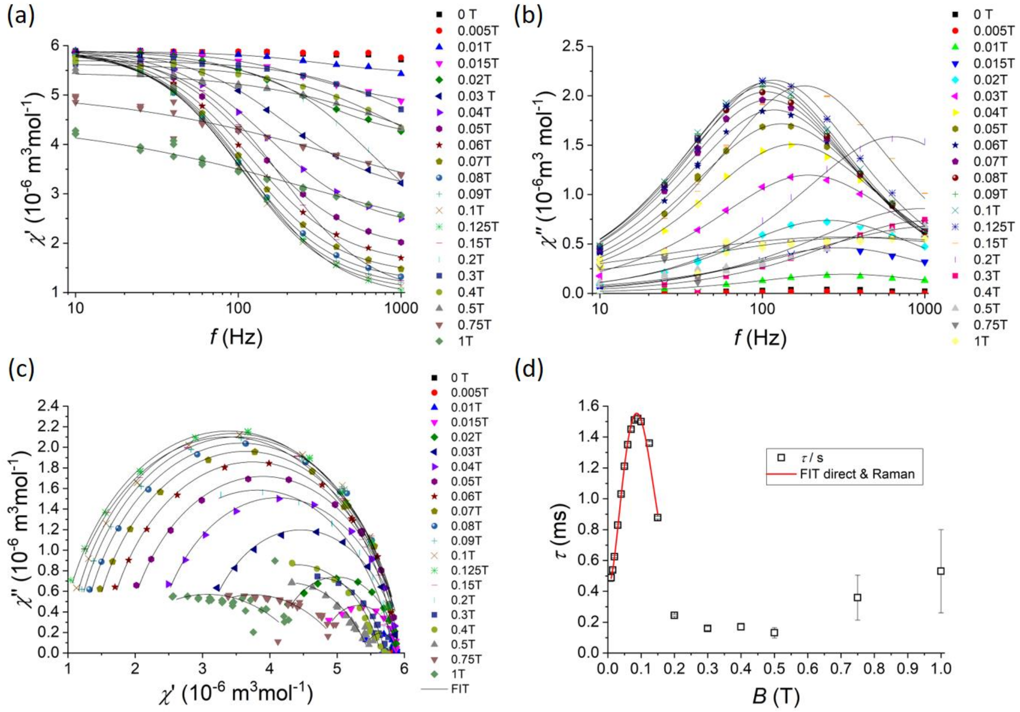

Fig. S35 AC susceptibility data for **2** recorded at various static magnetic fields at T = 2.0 K: Frequency dependent in-phase χ'(a) and out-of-phase χ''(b) component of AC susceptibility and Cole-Cole diagram (c) (solid lines are results of fits according to equations S1 and S2). (d) Field dependency of relaxation time.

Table S22 Parameters of the extended one-set Debye model (Eqs. S1 and S2) for **2** measured at 0.09 T

B (T)	**χ_T (10^{-6} cm^3 mol^{-1})**	**χ_S (10^{-6} cm^3 mol^{-1})**	**α (10^{-2})**	**τ (10^{-3} s)**	**R^2**
1.9	6.019(7)	1.11(2)	0.083(4)	1.5(1)	0.99975
2.1	5.785(5)	1.05(1)	0.089(3)	1.05(1)	0.99984
2.3	5.53(5)	1.01(1)	0.087(3)	1.26(7)	0.99986
2.5	5.324(4)	0.97(1)	0.089(3)	1.14(6)	0.99988
2.7	5.108(4)	0.94(1)	0.086(3)	0.99(5)	0.99987
2.9	4.909(4)	0.92(1)	0.078(3)	0.83(4)	0.99988
3.1	4.731(4)	0.89(1)	0.066(3)	0.63(4)	0.99986
3.3	4.551(3)	0.87(1)	0.048(3)	0.63(4)	0.99986
3.5	4.392(4)	0.85(3)	0.041(5)	0.24(3)	0.99983
3.7	4.240(2)	0.84(4)	0.046(2)	0.13(2)	0.99994
3.9	4.102(2)	0.95(1)	0.055(9)	0.08(4)	0.99992
4.1	3.982(3)	1.17(3)	0.084(2)	0.04(6)	0.9999

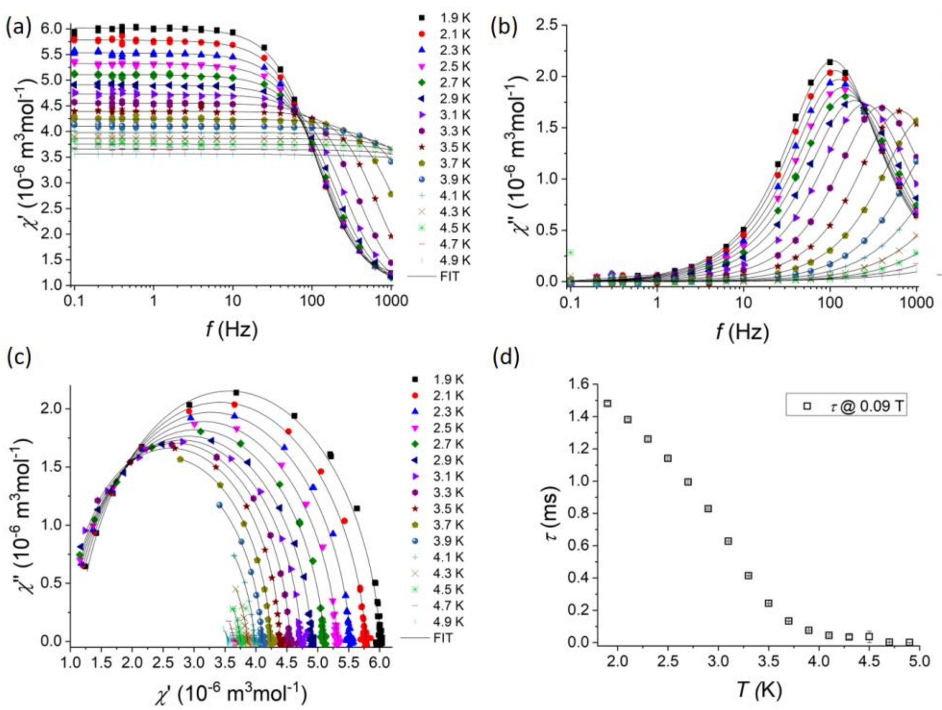

Fig. S36 AC susceptibility data for **2** recorded at various temperatures at 0.09 T: Frequency dependent in-phase χ'(a) and out-of-phase χ''(b) component of AC susceptibility and Cole-Cole diagram (c) (solid lines are results of fits according to equations S1 and S2). (d) Temperature dependency of relaxation time.

Table S23 Parameters of the extended one-set Debye model (Eqs. S1 and S2) for **2** measured at 0.125 T

B **(T)**	χ_T **(10^{-6} cm^3 mol^{-1})**	χ_S **(10^{-6} cm^3 mol^{-1})**	α **(10^{-2})**	τ **(10^{-3} s)**	R^2
1.9	6.000(7)	0.91(2)	0.087(4)	1.37(1)	0.99969
2.1	5.751(8)	0.87(2)	0.090(5)	1.31(1)	0.99961
2.3	5.52(1)	0.84(3)	0.090(6)	1.24(1)	0.99932
2.5	5.300(7)	0.81(2)	0.091(4)	1.15(9)	0.99964
2.7	5.03(4)	0.8(1)	0.07(3)	1.03(5)	0.98522
2.9	4.87(1)	0.78(4)	0.07(1)	0.87(2)	0.99804
3.1	4.74(5)	0.7(2)	0.07(4)	0.66(5)	0.97876
3.3	4.516(8)	0.76(4)	0.033(8)	0.43(6)	0.99923
3.5	4.355(9)	0.76(7)	0.02(1)	0.25(7)	0.99898
3.7	4.221(6)	0.8(1)	0.03(1)	0.14(5)	0.99959
3.9	4.05(1)	1.1(2)	0	0.096(8)	0.99741
4.1	3.963(7)	1.4(6)	0	0.06(4)	0.99944

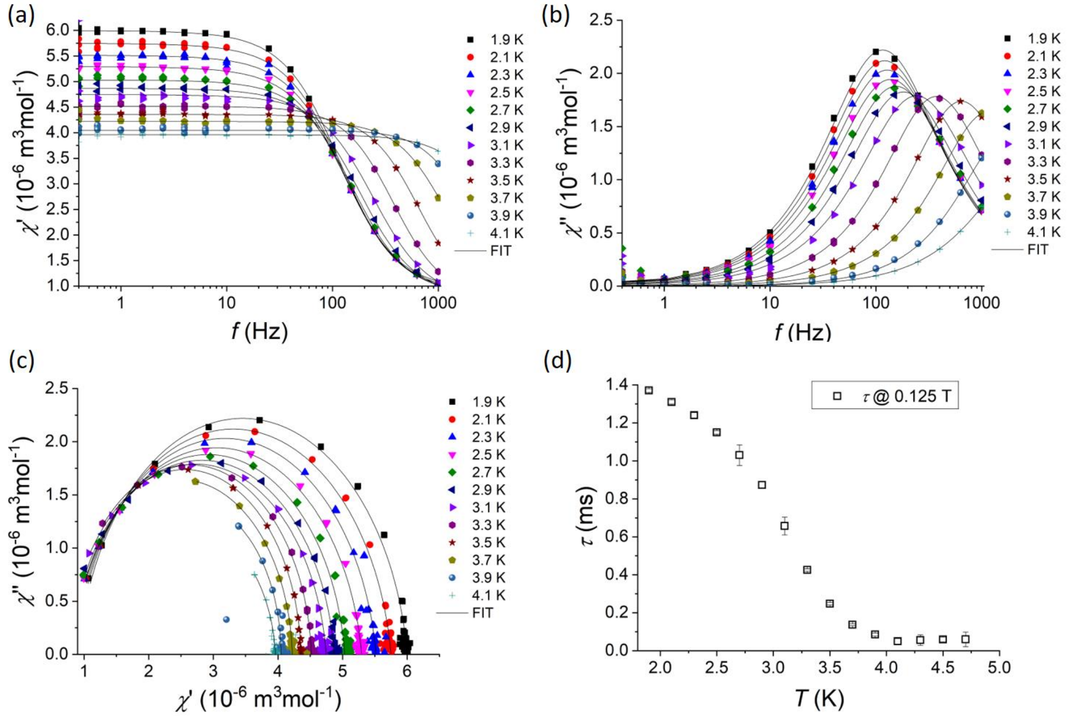

Fig. S37 AC susceptibility data for **2** recorded at various temperatures at 0.125 T: Frequency dependent in-phase χ'(a) and out-of-phase χ''(b) component of AC susceptibility and Cole-Cole diagram (c) (solid lines are results of fits according to Eqs. S1 and S2). (d) Temperature dependency of relaxation time τ.

Table S24 Relaxation parameters for compound **2** obtained by fitting of τ vs B dependency at T = 2 K using the respective combinations of Raman and direct relaxation processes

Model	***a*** **(*T*$^{-m}$ K^{-1} s^{-1})** ***m***	**2^n*d (s^{-1})**	***e*** **(K^{-2})** ***f*** **(K^{-2})**	**R^2**
Direct & Raman[a]	6.3(4) × 10^5 4 (fixed)	2308(43)	1488(133) 269(34)	0.99649

[a] for fields in the range 0 – 0.15 T

Table S25 Relaxation parameters at B_{DC} = 0.09 T for compound **2** using the respective combinations of Orbach and Raman relaxation processes

Model	***U*/*k*$_B$ (K)**	**τ_0 (s)**	***C*** **(K^{-n} s^{-1})** **n**	***aH^m*** **(K^{-1} s^{-1})**	***R*^{2}**
Orbach[a]	38(1)	4(2) × 10^{-9}	-	-	0.99428
Obach & direct	47.6(4)	4.3(5) × 10^{-10}	-	349(2)	0.99987
Raman & direct			2.4(8) × 10^{-4} 13.0(2)	340(5)	0.99932
Orbach & Raman	-	-	-	-	Not successful
Orbach & Raman & direct	47.6(9)	4(1) × 10^{-10}	2 × 10^{-12}±0.1 3.72±10^{11}	349(3)	0.99984

[a] for data in the range 3.3 – 4.1 K

Table S26 Relaxation parameters at B_{DC} = 0.125 T for compound **2** using the respective combinations of Orbach and Raman relaxation processes

Model	***U*/*k*$_B$ (K)**	**τ_0 (s)**	***C* (K^{-n} s^{-1})** **n**	***aH^m* (K^{-1} s^{-1})**	***R*^{2}**
Orbach[a]	36(1)	$8(2) \times 10^{-9}$	-	-	0.99669
Obach & direct	47(1)	$6(2) \times 10^{-9}$	-	352(7)	0.99844
Raman & direct			$2(2) \times 10^{-4}$ 12.8(6)	345(12)	0.99635
Orbach & Raman	-	-	-	-	Not successful
Orbach & Raman & direct	-	-	-	-	Not successful

[a] for data in the range 3.3 – 4.1 K

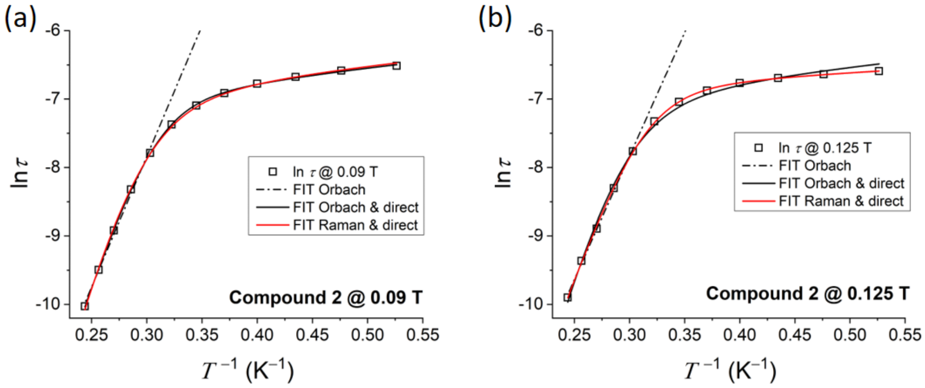

Fig. S38 ln *τ* vs 1/T dependencies fitted to the respective relaxation processes for **2** at two static magnetic fields.

Table S27 Relaxation parameters of compound **2** obtained from the simultaneous fit of two ln *τ* vs 1/T dependencies recorded at 0.09 T and 0.125 T DC fields

Model	***U*/*k*$_B$ (K)**	**τ_0 (s)**	**τ_{QTM}^{-1} (s^{-1})**	***a* (*T*$^{-m}$ K^{-1} s^{-1})** ***m***	***R*^{2}**
Orbach & QT	41(1)	$2.2(7) \times 10^{-9}$	789(19)	-	0.9961
Orbach & direct	36(7)	$(9\pm18)\times10^{-9}$	-	$2.3(4) \times 10^{6}$ 4 (fixed)	0.81558
Orbach & direct & QT	41(1)	$2.2(7) \times 10^{-9}$	776(33)	$4(8) \times 10^{4}$ 4 (fixed)	0.99595

Table S28 Comparison of structural, anisotropic and relaxation parameters for pseudotetrahedral cobalt(II) complexes

Compounds	***Structural parameters***	***D* / cm^{-1}**	***Relaxation parameters***	***ref***
[Co(L1)$_2$]	S(T$_d$)=1.82 τ_4=0.49	-36.7^m	U_{eff}=36 K; τ_0=5.6×10^{-10} s	[25]
[Co(L2)$_2$].CH$_2$Cl$_2$	S(T$_d$)=2.74 τ_4=0.44	-39.8^m	U_{eff}=43 K; τ_0=8.4×10^{-10} s	[25]
[Co(L3)$_2$]	S(T$_d$)=3.1 τ_4=0.49	-25.1^m -23.1^e -35.8^a	U_{eff}=48 K; τ_0=3.3×10^{-10} s C =0.85 K^{-n} s^{-1}; n=5.0 A = 6.4×10^{-9} s^{-1} Oe^{-4} K^{-1}	[26]
[Co(L4)$_2$]	S(T$_d$)=4.8 τ_4=0.48	-31.4^m -30.6^e -40.3^a	U_{eff}=76 K; τ_0=8×10^{-12} s C =6.6×10^{-4} K^{-n} s^{-1}; n=9.0	[26]
[Co(L5)$_2$].C$_2$H$_6$O	S(T$_d$)=1.60 τ_4=0.48	-19.3^m -26.1^a	U_{eff}=48 K, τ_0 = 6.8×10^{-10} s τ_{QTM}=0.012 s	[27]
[Co(L6)$_2$].C$_2$H$_6$O	S(T$_d$)=1.33 τ_4=0.48	-19.2^m -24.1^a	U_{eff}=47 K, τ_0=2.0×10^{-10} s τ_{QTM}=0.0035	[27]
[Co(L7)$_2$]	S(T$_d$)=2.9 τ_4=0.44	-41^m	U_{eff}=49 K, τ_0=7.5×10^{-8} s	[28]

^{m}magnetic data analysis; ^{e}HFEPR; ^{a}*ab initio*; S(T_d) – tetrahedral symmetry measure parameter [29]–[31], τ_4 [32], **L1**=1-[N-(4-Bromophenyl)carboximidoyl]naphthalen-2-ol; **L2**=1-[N-(2-Phenylphenyl)carboximidoyl]naphthalen-2-ol; **L5**=2-(Adamantan-1-ylimino)methyl-4- methylphenol; **L3**=2-(([1,1 ’ -biphenyl]-2-ylimino)methyl)phenol; **L4**= 1-(([1,1’-biphenyl]-2-ylimino)methyl(2-(([1,1’-biphenyl]-2-ylimino)methyl)phenol); **L6**=2-(Adamantan-1-ylimino)methyl-4- bromophenol; **L7**=2-(4,5-diphenyl-1H-imidazol-2- yl)phenol.

Section S8. Electric Transport Measurements

To perform electric transport measurements of deposited samples on graphene, the compounds were drop-cast onto graphene field-effect transistors (GFETs). The preparation of the devices was as follows. Graphene was grown by chemical vapor deposition on Cu foil (Sigma Aldrich), and wet-transferred onto Si/SiO2 wafers. (p-doped (100) Si with 3000 Å dry thermal oxide from University Wafer – South Boston, MA, USA). Standard photolithography methods were used to pattern the graphene into Hall-bar geometries. Cr/Au contact pads were deposited by magnetron sputtering (15 Å Cr and 4000 Å Au). The clean devices were vacuum annealed at 140°C for 1 hr before electrical measurements were taken using a probe station in ambient conditions. Powder samples of 1 and 2 were dissolved in acetone to make 0.1 mM solutions. Directly after measuring the clean devices, the solutions were drop-cast via a syringe onto the clean devices. The solvent was given about 30 s to evaporate and electrical measurements were then taken on the coated devices.

The gate-dependent conductance of the deposited compound **2** on a GFET is shown in Fig. 5e of the main text. It shows a clear shift of the charge neutrality point (conductivity minimum) towards a lower gate voltage, demonstrating n-doping of graphene after deposition. Fig. S39 shows the results for compound **1**, the charge neutrality point also shifts to a lower gate voltage, although not as markedly as in compound **2.** We conclude that the charge transfer effect may be much weaker with **1**, or a lower coverage of the devices may have muted the effect.

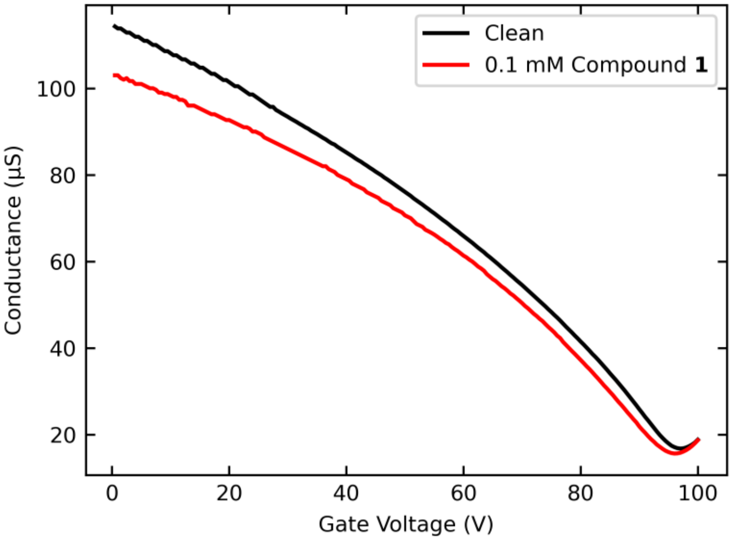

Fig. S39 Gate-dependent conductivity through GFETs before and after deposition of Compound **1** by drop-cast.

Section S9. Plane-Wave DFT Calculations: Supercell Size, Charge Density Difference, and Density of States Analysis

Supercell Size

Fig. S40 shows the size and shape of the supercell used in plane-wave DFT calculations. The size and shape was kept constant in all calculations, namely, on the isolated molecule, isolated substrate, and molecule + substrate systems.

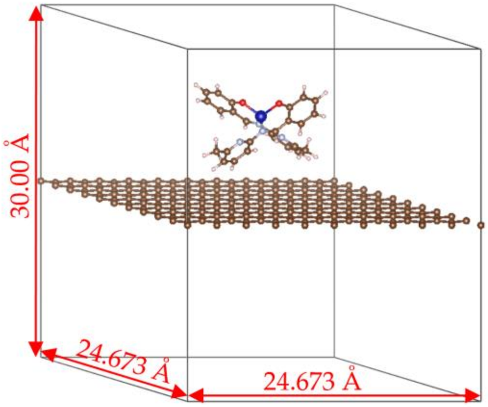

Fig. S40 Supercell used for plane-wave DFT calculations. As an example, compound **1** in configuration 1 is shown.

Charge Density Difference

Analysis of the charge density difference allows to study the charge transfer behavior of the molecule + substrate system. The charge density difference is defined as:

$$\Delta\rho = \rho_{\mathrm{mol+subs}} - \rho_{\mathrm{mol}} - \rho_{\mathrm{subs}},$$

with $\rho_{\mathrm{mol+subs}}$, ρ_{mol}, and ρ_{subs} the charge density of the molecule + substrate, isolated molecule, and isolated substrate, respectively. The insets of Figs. S41a-d and S42a-d show isosurface plots of the charge density difference plots of compounds **1** and **2**, respectively, in all configurations. The isosurface plots show that in configurations 1 and 3 of both compounds, there is a charge accumulation near the graphene substrate and an overall depletion in the molecule. **Confs 2**, **4** of both compounds show a more complex behavior, with regions of both depletion and accumulation in molecule and substrate. A clearer description of the charge transfer dynamics can be obtained by the planar average of the charge density difference, that is, by averaging $\Delta\rho$ in the plane perpendicular to the z axis (xy plane). The planar averaging procedure was performed using the VASPKIT software [33]. The planar average plots, shown in Fig. S41a-d and S42a-d, evidence a similar behavior for each configuration of both compounds, and as mentioned before, **Confs. 1**, **3** show a clear charge accumulation near graphene (located at position z = 15 Å). In **Confs. 2**, **4** regions of charge accumulation in the molecule are observed (for instance, at position z = 18 Å), which correspond to the positions of the H atoms.

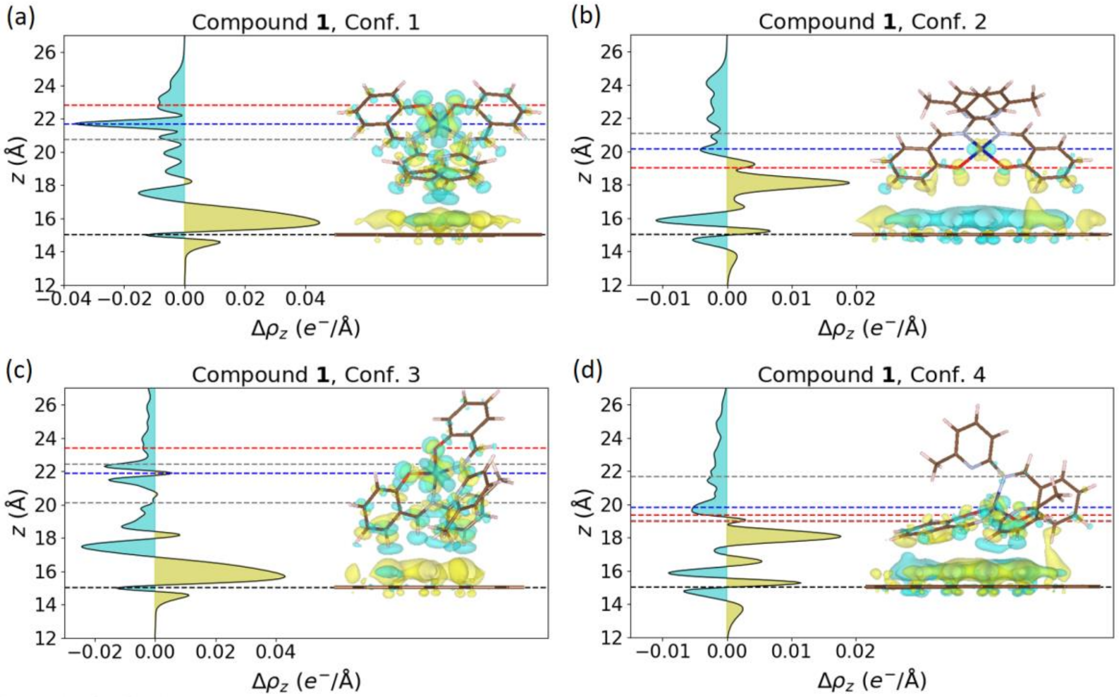

Fig. S41 (a-d) Planar average (along the xy plane) of the charge density for each configuration of compound **1**. Superimposed on each plot are isosurface plots of the charge density difference, with isosurface level $1.01\times 10^{-3}\ e^-/\text{Å}^3$ ($1.5\times 10^{-4}\ e^-/\text{Bohr}^3$). Yellow and cyan colors represent charge accumulation and depletion, respectively. The dashed black, blue, red, and grey lines correspond to the vertical location of graphene, the Co, O, and coordinating N atoms, respectively.

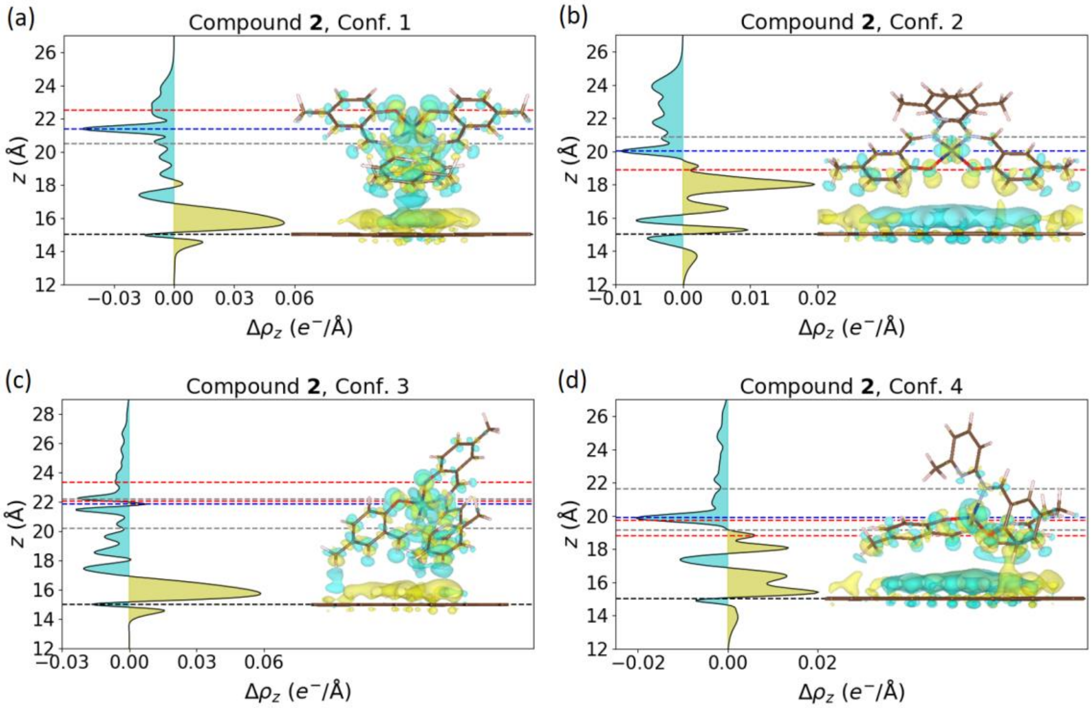

Fig. S42 (a-d) Planar average (along the *xy* plane) of the charge density for each configuration of compound **2**. Superimposed on each plot are isosurface plots of the charge density difference, with isosurface level $1.01\times 10^{-3}\, e^-/\text{Å}^3$ ($1.5 \times 10^{-4}\, e^-/\text{Bohr}^3$). Yellow and cyan colors represent charge accumulation and depletion, respectively. The dashed black, blue, red, and grey lines correspond to the vertical location of graphene, the Co, O, and coordinating N atoms, respectively.

Density of States Analysis

As discussed in the main text, analysis of the density of states (DOS) corroborated the charge transfer from molecule to substrate, showing an electron transfer from the molecule's HOMO to graphene's conduction band. This behavior is consistent in both compounds in all configurations, as showed in the partial DOS (PDOS) plots of Figs. S43 and S44. The PDOS was obtained by calculating the DOS of each molecule + substrate system, and then selecting the atoms of molecule and substrate separately, considering the contribution from all atomic orbitals (*s*, *p*, and in Co case, *d* orbitals).

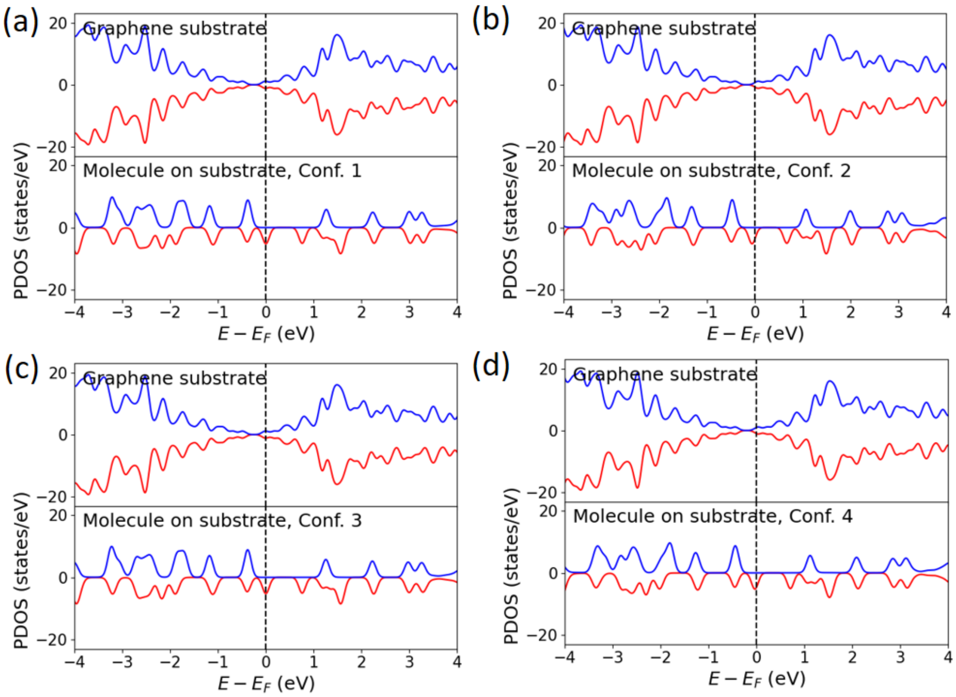

Fig. S43 Partial density of states (PDOS) of compound 1 in different configurations on graphene. (a-d) configs. 1 to 4, respectively.

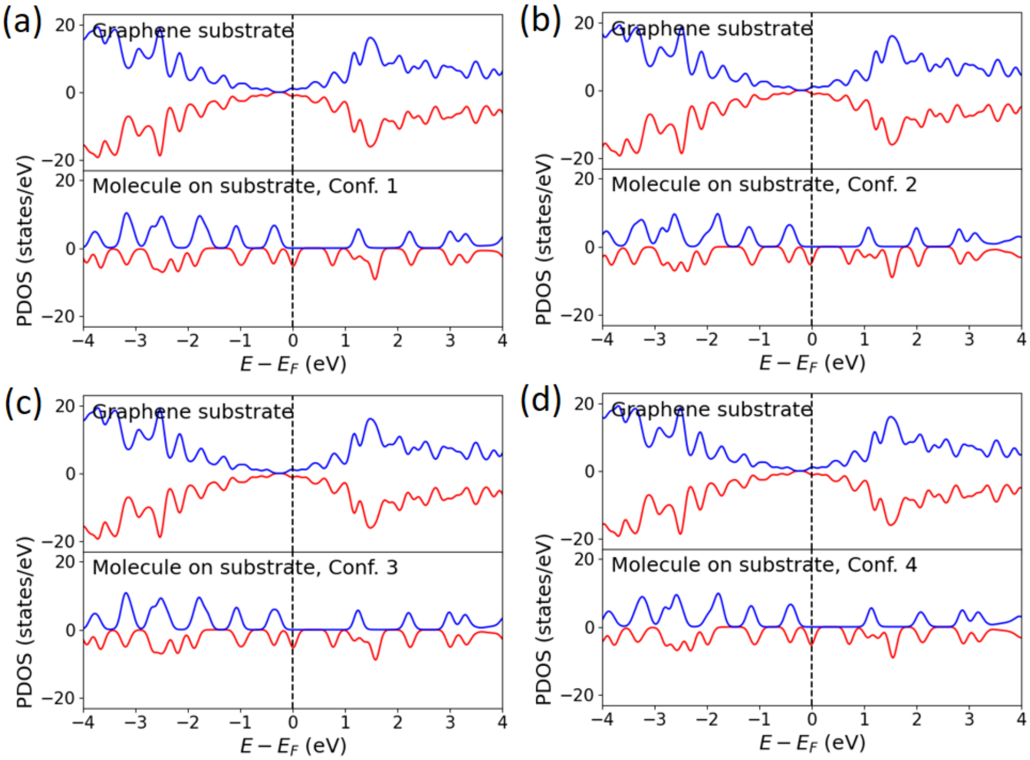

Fig. S44 Partial density of states (PDOS) of compound **2** in different configurations on graphene. (a-d) configs. 1 to 4, respectively.

References

[1] G. M. Sheldrick, “Crystal structure refinement with SHELXL,” *Acta Crystallogr. C*, vol. 71, no. 1, pp. 3–8, Jan. 2015.

[2] L. J. Bourhis, O. V. Dolomanov, R. J. Gildea, J. A. K. Howard, and H. Puschmann, “The anatomy of a comprehensive constrained, restrained refinement program for the modern computing environment - Olex2 dissected,” *Acta Crystallogr. A*, vol. 71, no. 1, pp. 59–75, Jan. 2015.

[3] O. V. Dolomanov, L. J. Bourhis, R. J. Gildea, J. A. K. Howard, and H. Puschmann, “OLEX2: A complete structure solution, refinement and analysis program,” *J. Appl. Crystallogr.*, vol. 42, no. 2, pp. 339–341, Jan. 2009.

[4] D. Jayatilaka and B. Dittrich, “X-ray structure refinement using aspherical atomic density functions obtained from quantum-mechanical calculations,” *Acta Crystallogr.A*, vol. 64, no. 3, pp. 383–393, Apr. 2008.

[5] S. C. Capelli, H. B. Bürgi, B. Dittrich, S. Grabowsky, and D. Jayatilaka, “Hirshfeld atom refinement,” *IUCrJ*, vol. 1, pp. 361–379, Aug. 2014.

[6] F. Kleemiss *et al.*, “Accurate crystal structures and chemical properties from NoSpherA2,” *Chem. Sci.*, vol. 12, no. 5, pp. 1675–1692, Feb. 2021.

[7] C. F. MacRae *et al.*, “Mercury 4.0: From visualization to analysis, design and prediction,” *J. Appl. Crystallogr.*, vol. 53, no. 1, pp. 226–235, Feb. 2020.

[8] L. Xu, Y. V. Mironov, X. Qi, and S. J. Kim, “A new Co(II) complex with N,O-donor Schiff base: Synthesis, structure and characterization,” *J. Struct. Chem.*, vol. 47, no. 5, pp. 998–1001, Sep. 2006.

[9] S. Stoll and A. Schweiger, “EasySpin, a comprehensive software package for spectral simulation and analysis in EPR,” *J. Magn. Reson.*, vol. 178, no. 1, pp. 42–55, Jan. 2006.

[10] R. Boča, *Theoretical Foundations of Molecular Magnetism*, First edit. Amsterdam: Elsevier, 1999.

[11] A. Sojka *et al.*, “Sample Holders for Sub-THz Electron Spin Resonance Spectroscopy,” *IEEE T. Instrum. Meas.*, vol. (Accepted), 2022.

[12] V. Mankad, S. K. Gupta, P. K. Jha, N. N. Ovsyuk, and G. A. Kachurin, “Low-frequency Raman scattering from Si/Ge nanocrystals in different matrixes caused by acoustic phonon quantization,” *J. Appl. Phys.*, vol. 112, no. 5, 2012.

[13] P. G. Spizzirri, J. H. Fang, S. Rubanov, E. Gauja, and S. Prawer, “Nano-Raman spectroscopy of silicon surfaces,” *Mater. Forum*, vol. 34, pp. 161–166, 2008.

[14] A. C. Ferrari, “Raman spectroscopy of graphene and graphite: Disorder, electron–phonon coupling, doping and nonadiabatic effects,” *Solid State Commun.*, vol. 143, no. 1–2, pp. 47–57, Jul. 2007.

[15] A. C. Ferrari and D. M. Basko, “Raman spectroscopy as a versatile tool for studying the properties of graphene,” *Nat. Nanotechnol.*, vol. 8, no. 4, pp. 235–246, Apr. 2013.

[16] G. Socrates, *Infrared and Raman characteristic group frequencies: tables and charts*, 3rd ed. John Wiley & Sons, 2004.

[17] D. A. Shirley, “High-resolution x-ray photoemission spectrum of the valence bands of gold,” *Phys. Rev. B*, vol. 5, no. 12, pp. 4709–4714, 1972.

[18] J. Hrubý *et al.*, “Deposition of Tetracoordinate Co(II) Complex with Chalcone Ligands on Graphene,”

Molecules, vol. 25, no. 21, p. 5021, Oct. 2020.

[19] J. Hrubý *et al.*, “Co(ii)-Based single-ion magnets with 1,1′-ferrocenediyl-bis(diphenylphosphine) metalloligands,” *Dalton Trans.*, vol. 49, no. 33, pp. 11697–11707, Sep. 2020.

[20] R. Podila, J. Chacón-Torres, J. T. Spear, T. Pichler, P. Ayala, and A. M. Rao, “Spectroscopic investigation of nitrogen doped graphene,” *Appl. Phys. Lett.*, vol. 101, no. 12, p. 123108, Sep. 2012.

[21] J. J. Yeh and I. Lindau, “Atomic subshell photoionization cross sections and asymmetry parameters: $1 \leq Z \leq 103$,” *At. Data Nucl. Data Tables*, vol. 32, no. 1, pp. 1–155, 1985.

[22] G. Poneti *et al.*, “Magnetic and spectroscopic investigation of thermally and optically driven valence tautomerism in thioether-bridged dinuclear cobalt-dioxolene complexes,” *Inorg. Chem.*, vol. 52, no. 20, pp. 11798–11805, Oct. 2013.

[23] S. Biniak, G. Szymański, J. Siedlewski, and A. Światkoski, “The characterization of activated carbons with oxygen and nitrogen surface groups,” *Carbon N. Y.*, vol. 35, no. 12, pp. 1799–1810, 1997.

[24] J. Lahaye, G. Nansé, A. Bagreev, and V. Strelko, “Porous structure and surface chemistry of nitrogen containing carbons from polymers,” *Carbon N. Y.*, vol. 37, no. 4, pp. 585–590, 1999.

[25] S. Ziegenbalg, D. Hornig, H. Görls, and W. Plass, “Cobalt(II)-Based Single-Ion Magnets with Distorted Pseudotetrahedral [N2O2] Coordination: Experimental and Theoretical Investigations,” *Inorg. Chem.*, vol. 55, no. 8, pp. 4047–4058, May 2016.

[26] M. Böhme, S. Ziegenbalg, A. Aliabadi, A. Schnegg, H. Görls, and W. Plass, “Magnetic relaxation in cobalt(ii)-based single-ion magnets influenced by distortion of the pseudotetrahedral [N2O2] coordination environment,” *Dalton Trans.*, vol. 47, no. 32, pp. 10861–10873, 2018.

[27] G. Peng, Y. Chen, B. Li, Y.-Q. Zhang, and X.-M. Ren, “Bulky Schiff-base ligand supported Co(<scp>ii</scp>) single-ion magnets with zero-field slow magnetic relaxation,” *Dalton Trans.*, vol. 49, no. 18, pp. 5798–5802, 2020.

[28] A. Buchholz, A. O. Eseola, and W. Plass, “Slow magnetic relaxation in mononuclear tetrahedral cobalt(II) complexes with 2-(1H-imidazol-2-yl)phenol based ligands,” *Comptes Rendus Chim.*, vol. 15, no. 10, pp. 929–936, Oct. 2012.

[29] S. Grimme, S. Ehrlich, and L. Goerigk, “Effect of the damping function in dispersion corrected density functional theory,” *J. Comput. Chem.*, vol. 32, no. 7, pp. 1456–1465, May 2011.

[30] J. Neugebauer and M. Scheffler, “Adsorbate-substrate and adsorbate-adsorbate interactions of Na and K adlayers on Al(111),” *Phys. Rev. B*, vol. 46, no. 24, pp. 16067–16080, Dec. 1992.

[31] G. Makov and M. C. Payne, “Periodic boundary conditions in *ab initio* calculations,” *Phys. Rev. B*, vol. 51, no. 7, pp. 4014–4022, Feb. 1995.

[32] L. Yang, D. R. Powell, and R. P. Houser, “Structural variation in copper(<scp>i</scp>) complexes with pyridylmethylamide ligands: structural analysis with a new four-coordinate geometry index, τ_4,” *Dalton Trans.*, no. 9, pp. 955–964, 2007.

[33] V. Wang, N. Xu, J. C. Liu, G. Tang, and W. T. Geng, “VASPKIT: A user-friendly interface facilitating high-throughput computing and analysis using VASP code,” *Comput. Phys. Commun.*, vol. 267, p. 108033, Oct. 2021.